Article

A remnant planetary core in the hot-Neptune desert

https://doi.org/10.1038/s41586-020-2421-7

Received: 29 October 2019

Accepted: 20 March 2020

Published online: 1 July 2020

Check for updates

A list of authors and their affililations appears at the end of the paper.

The interiors of giant planets remain poorly understood. Even for the planets in the Solar System, difficulties in observation lead to large uncertainties in the properties of planetary cores. Exoplanets that have undergone rare evolutionary processes provide a route to understanding planetary interiors. Planets found in and near the typically barren hot-Neptune 'desert'[1,2] (a region in mass–radius space that contains few planets) have proved to be particularly valuable in this regard. These planets include HD149026b[3], which is thought to have an unusually massive core, and recent discoveries such as LTT9779b[4] and NGTS-4b[5], on which photoevaporation has removed a substantial part of their outer atmospheres. Here we report observations of the planet TOI-849b, which has a radius smaller than Neptune's but an anomalously large mass of $39.1^{+2.7}_{-2.6}$ Earth masses and a density of $5.2^{+0.7}_{-0.8}$ grams per cubic centimetre, similar to Earth's. Interior-structure models suggest that any gaseous envelope of pure hydrogen and helium consists of no more than $3.9^{+0.8}_{-0.9}$ per cent of the total planetary mass. The planet could have been a gas giant before undergoing extreme mass loss via thermal self-disruption or giant planet collisions, or it could have avoided substantial gas accretion, perhaps through gap opening or late formation[6]. Although photoevaporation rates cannot account for the mass loss required to reduce a Jupiter-like gas giant, they can remove a small (a few Earth masses) hydrogen and helium envelope on timescales of several billion years, implying that any remaining atmosphere on TOI-849b is likely to be enriched by water or other volatiles from the planetary interior. We conclude that TOI-849b is the remnant core of a giant planet.

The TESS mission[7] observed the star TOI-849/TIC33595516 (V magnitude 12) for 27 days during September and October 2018, leading to the detection of a candidate transiting planet. TOI-849 was observed at a cadence of 30 min in the full-frame images using the MIT Quick Look pipeline (see Methods). No signs of additional planets or stellar activity were seen in the photometry. Follow-up observations with the HARPS spectrograph detected a large radial velocity signal, confirming the planet TOI-849b. Four additional transits were observed using the ground-based telescopes Next Generation Transit Survey[8] and Las Cumbres Observatory Global Telescope[9], improving the radius determination and ephemeris of the planet. A search in Gaia Data Release 2 reveals no other sources closer than 39″, with the closest source being 7.8 magnitudes fainter than TOI-849 in the G band[10]. Additional high-resolution imaging from SOAR, NACO/VLT, AstraLux and Zorro/Gemini South revealed no unresolved companion stars. We perform a joint fit to the data using the PASTIS software[11] to extract planetary and stellar parameters, using the combined HARPS spectra to derive priors on the stellar parameters and calculate chemical abundances for the host star (see Methods). The best fit and data are shown in Fig. 1.

TOI-849b has a mass of $39.1^{+2.7}_{-2.6} M_\oplus$ ($M_\oplus$, mass of Earth), nearly half the mass of Saturn (all uncertainties are 1σ unless otherwise stated). The planet's radius is $3.44^{+0.16}_{-0.12} R_\oplus$ ($R_\oplus$, Earth radius) and its mean density is $5.2^{+0.7}_{-0.8}$ g cm^{-3}, making it the densest Neptune-sized planet discovered so far (Fig. 2). It has an orbital period of 0.7655241 ± 0.0000027 d, making it an 'ultrashort-period' planet. The upper limit on its eccentricity is 0.08 at 95% confidence. Its radius, mass and period place TOI-849b in the middle of the hot-Neptune desert, a region of parameter space typically devoid of planets due to photoevaporation and tidal disruption[1,2] (Fig. 3). The host star TOI-849 is a late G dwarf with mass $(0.929 \pm 0.023) M_\odot$, radius $0.919^{+0.029}_{-0.023} R_\odot$ ($M_\odot$ and $R_\odot$ are the mass and radius of the Sun, respectively) and age $6.7^{+2.9}_{-2.4}$ Gyr. The close proximity of the planet and the star lead to an equilibrium temperature of 1,800 K for the planet, assuming an albedo of 0.3. The full set of derived parameters for the planet and star are given in Extended Data Tables 1, 2 and general stellar parameters are provided in Extended Data Table 3.

The most widely used interior-structure models for terrestrial planets are not valid for planets as massive as TOI-849b, because the properties of matter at such high central pressures remain highly uncertain. Furthermore, some compositional mixing is expected at these high pressures and temperatures[12], in contradiction of the usual assumption of distinct layers[13]. We build an internal-structure model accounting for some of these issues (see Methods), but restrict our analysis to the limiting cases of a maximum and minimum possible hydrogen and helium (H/He) envelope mass under the layered-structure assumption. We calculate the maximum envelope mass by minimizing the contribution of the core, mantle and water, assuming that the planet has the same [Fe/Si] ratio as that observed for the photosphere of the host star. Under this model, the maximum envelope mass fraction is $3.9^{+0.8}_{-0.9}$%.

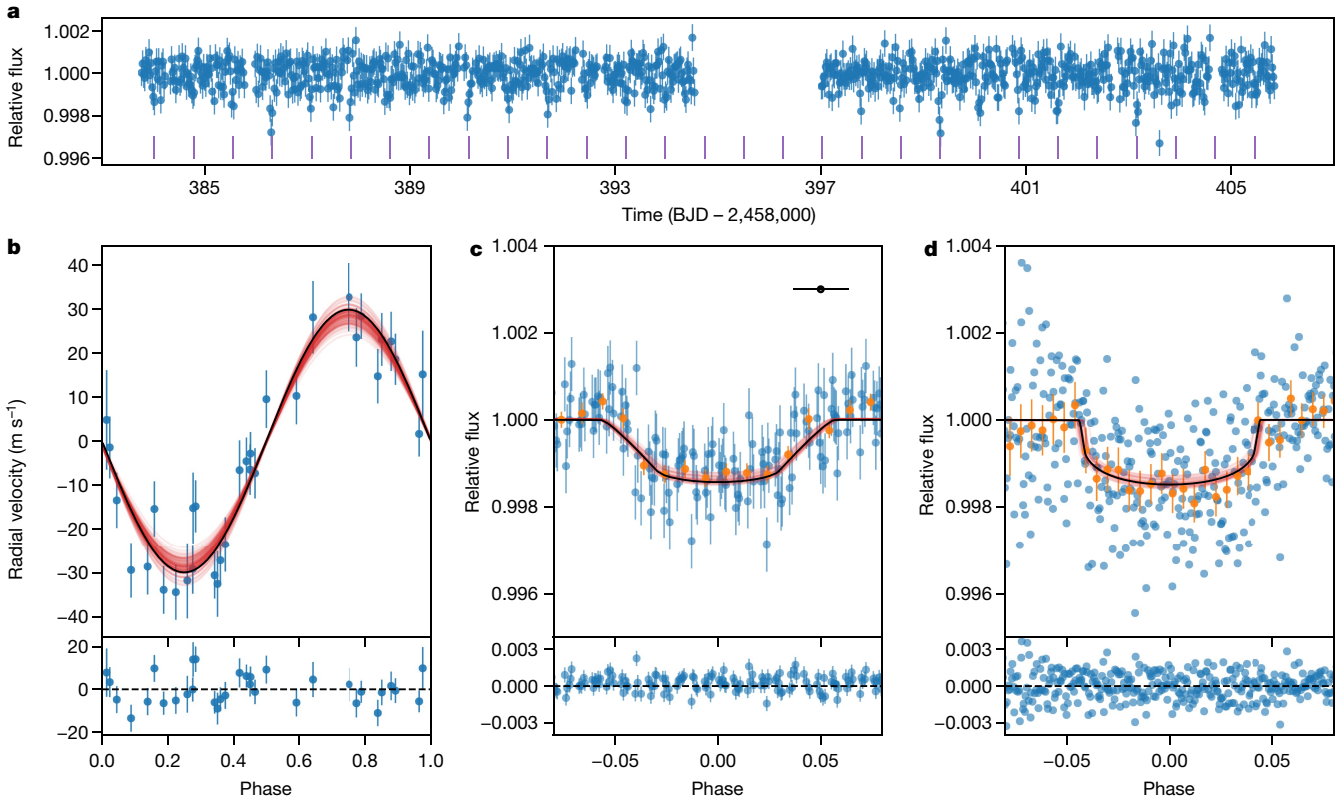

Fig. 1 | Best-fitting model to the TESS, HARPS and NGTS data. a, TESS light curve with transit times marked as vertical lines. BJD, barycentric Julian date. **b**, Phase-folded HARPS data (blue symbols) and best-fitting model (black line), with residuals shown in the bottom panel. Several models randomly drawn from the Markov chain Monte Carlo output are shown in red. **c**, Phase-folded TESS 30-min cadence data (blue symbols) and binned to 0.01 in phase (orange symbols, nine individual points per bin), with models as in **b** and residuals shown in the bottom panel. The horizontal error bar shows the TESS cadence. **d**, Phase-folded NGTS data binned to 1 min (blue symbols, 46 individual points per bin) and to 0.01 in phase (orange symbols, 777 individual points per bin). We plot the binned NGTS data to aid visualization but we fit the models to the full dataset. Models are as in **b**, with residuals in the bottom panel. The cadence is negligible at this scale. Data from Las Cumbres Observatory Global Telescope were also used and are shown in Extended Data Fig. 1. Vertical error bars of individual points show one standard deviation. In the case of binned measurements, points and error bars show the weighted mean and its standard error, respectively.

The large core mass and low envelope mass fraction of TOI-849b challenge the traditional view of planet formation via core accretion, in which planets with masses above a critical mass of about $10M_{\oplus}$–$20M_{\oplus}$ are expected to undergo runaway gas accretion within the protoplanetary disk[14–16]. Why, then, does TOI-849b lack a massive gaseous envelope? Apparently the core somehow avoided runaway accretion, or else the planet was once a gas giant that somehow lost most of its envelope. If runaway accretion proceeded to produce a giant planet, removal of most of the original mass would be required to reach the present-day state. HD149026b[3] is a giant planet with mass $(121 \pm 19)M_{\oplus}$ (ref. [17]), which is thought to have a solid core with a mass of about $50M_{\oplus}$ (refs. [18,19]), similar to TOI-849b. Starting from a planet such as HD149026b, a mass loss of 60–70% would be required to produce the present-day TOI-849b. Considering the proximity of TOI-849b to its host star, one would expect some mass loss to photoevaporation. The predicted lifetime mass-loss rate for a Jupiter-like planet is only a few per cent, well below the required range (see Methods). For a planet such as HD149026b, the situation is less clear, and the lifetime mass removed depends critically on the assumptions made. We proceed to explore several formation pathways for TOI-849b.

Tidal disruption could cause a mass loss of 1–2 orders of magnitude. The close proximity of a number of hot Jupiters to their tidal disruption radii[20] and the fact that hot Jupiters are preferentially found around younger stars[21,22] suggest that tidal disruption of hot Jupiters might be frequent. Although it appears that they do not typically leave behind a remnant core, or such cores are short-lived[23], as a rare higher-mass object, TOI-849b may be an unusual case. At the location of TOI-849b, tidal disruption would be expected for a Jupiter-mass planet with radius greater than 1.5 Jupiter radii. An alternative related pathway to substantial envelope loss is disruption via tidal thermalization events, which can lead to mass loss of 1–2 orders of magnitude. If TOI-849b reached its close orbit via high-eccentricity scattering by another planet in the system, energy buildup in the planet's internal f-modes during tidal circularization could approach large fractions of the planet's internal binding energy and potentially lead to thermalization events, which may remove envelope layers (see Methods). However, in either case it is unclear whether a giant planet could harbour a large enough core to leave behind a $40M_{\oplus}$ remnant, because the gaseous envelope on top of a core of a few Earth masses causes planetesimals to be eroded in the envelope. The remaining solids must subsequently rain out to produce such a large core[12,24,25].

Giant planet collisions provide another, intermediate way to produce planets similar to TOI-849b. The Bern planetary population synthesis models[26] predict the existence of a small population of planets with similar masses and semi-major axes to TOI-849b (see Methods). In those models, such planets are produced via giant planet collisions at the end of the migration phase, resulting in the ejection of the planetary envelope, leaving no time for the remnant core to accrete further gas. In these scenarios, the cores reach an envelope mass fraction of a few tens of per cent before being reduced to Neptune size and ejecting the envelope through an impact. Such a scenario leaves a dense planetary core close to the host star.

The alternative hypothesis is that TOI-849b avoids runaway accretion, possibly through opening a gap in the protoplanetary disk that is largely devoid of gas, before the planet accretes much envelope mass.

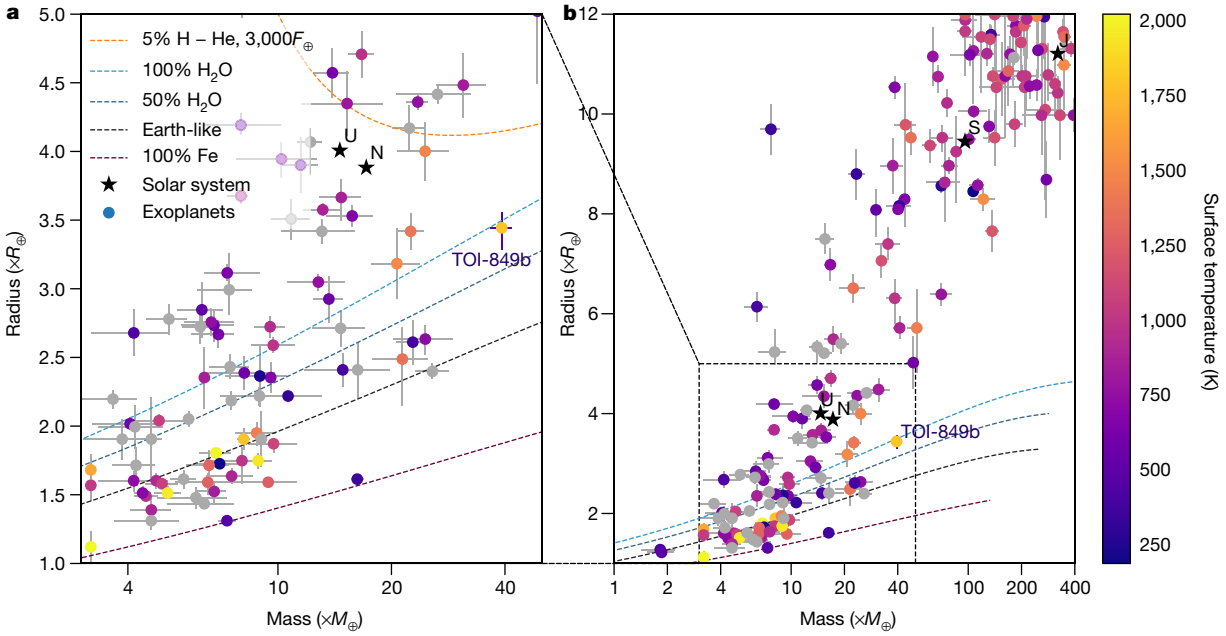

Fig. 2 | Mass–radius diagram of known exoplanets from the NASA exoplanet archive. a, **b**, The archive (https://exoplanetarchive.ipac.caltech.edu/) was accessed on 20 January 2020. Planets are coloured according to calculated equilibrium temperature and are grey otherwise. Planets with mass determinations better than 4σ are shown. Planets without a reported mass determination were excluded[30]. Composition tracks[31] are shown as dashed lines, with an additional 5% H–He track at an irradiation level similar to that of TOI-849b. U, N, S and J denote the Solar System planets Uranus, Neptune, Saturn and Jupiter, respectively. $F_\oplus$ represents the average solar irradiation received by Earth. **a**, Zoom of **b**. All error bars show one standard deviation.

Because the threshold mass required for a planet to open up a gap in a protoplanetary disk is sensitive to the disk scale height, which is small close to the star, planets on close-in orbits can more easily open a deep gap. A 40$M_\oplus$ planet such as TOI-849b on an orbit of 0.1 AU would reduce the disk surface density at its location by a factor about 10 (refs. [27,28]). Recently, it has been argued that a reduction in gas accretion due to gap opening is required to resolve the fact that runaway gas accretion models tend to produce too many Jupiter-mass planets and not enough sub-Saturn-mass planets[6]. Indeed, by reducing the accretion rate onto gap-opening planets, it is possible to produce 40$M_\oplus$ planets at 0.1 AU with gas mass fractions below 10% if the planets form late enough[6]. In contrast to the tidal disruption pathway, reduced gas accretion should leave TOI-849b aligned with the stellar spin axis. Detecting or ruling out such alignment using measurements of the Rossiter–McLaughlin effect[29], as well as taking measurements of the atmospheric composition, may aid in distinguishing between the various formation scenarios.

In all cases, remaining hydrogen and helium envelope masses of a few per cent could be removed over several billion years by photoevaporation, given the planet's close orbit. We estimate the current mass-loss rate to be 0.95$M_\oplus$ Gyr^{-1} (see Methods), which implies that an envelope mass of ~4% could be removed in a few billion years. Therefore, the question changes: where does TOI-849b's minor envelope come from? Given the high equilibrium temperature, we would expect that some ices would be evaporated to provide a secondary enriched atmosphere containing water and other volatiles. In these circumstances, TOI-849b provides a unique target in which the composition of a primordial planetary core could be studied by observing its atmospheric constituents with, for example, the Hubble Telescope or the upcoming James Webb Space Telescope.

The proximity of TOI-849b to its host star, which promotes gap opening and increases the role of photoevaporation, could explain why similar objects have not yet been found. Ultimately, however TOI-849b formed, the planet's large mass and low gas mass fraction will provide a stringent test of planet formation theory. TOI-849b gives us a glimpse at a core similar to those that exist at the centres of giant planets, exposed through an unlikely combination of inhibited accretion or mass loss.

Online content

Any methods, additional references, Nature Research reporting summaries, source data, extended data, supplementary information, acknowledgements, peer review information; details of author contributions and competing interests; and statements of data and code availability are available at https://doi.org/10.1038/s41586-020-2421-7.

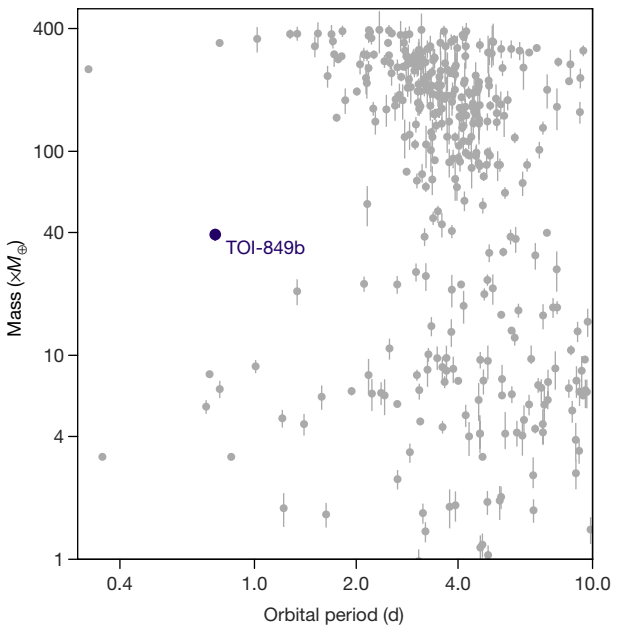

Fig. 3 | TOI-849b in the context of the hot-Neptune desert. Known exoplanets are plotted in grey and were sourced from the NASA exoplanet archive (https://exoplanetarchive.ipac.caltech.edu/) on 20th January 2020. Only planets with mass determinations better than 4σ are plotted. All error bars show one standard deviation.

1. Szabó, G. M. & Kiss, L. L. A short-period censor of sub-Jupiter mass exoplanets with low density. *Astrophys. J. Lett.* **727**, L44 (2011).
2. Owen, J. E. & Lai, D. Photoevaporation and high-eccentricity migration created the sub-Jovian desert. *Mon. Not. R. Astron. Soc.* **479**, 5012–5021 (2018).
3. Sato, B. et al. The N2K Consortium. II. A transiting hot Saturn around HD 149026 with a large dense core. *Astrophys. J.* **633**, 465–473 (2005).
4. Jenkins, J. TESS Discovery of the first ultra hot Neptune, LTT9779b. In *AAS/Division for Extreme Solar Systems Abstracts* Vol. 51, 103.07 (American Astronomical Society, 2019).
5. West, R. G. et al. NGTS-4b: a sub-Neptune transiting in the desert. *Mon. Not. R. Astron. Soc.* **486**, 5094–5103 (2019).
6. Lee, E. J. The boundary between gas-rich and gas-poor planets. *Astrophys. J.* **878**, 36 (2019).
7. Ricker, G. R. et al. Transiting exoplanet survey satellite (TESS). *J. Astron. Telesc. Instrum. Syst.* **1**, 014003 (2014).
8. Wheatley, P. J. et al. The next generation transit survey (NGTS). *Mon. Not. R. Astron. Soc.* **475**, 4476–4493 (2018).
9. Brown, T. M. et al. Las Cumbres Observatory global telescope network. *Publ. Astron. Soc. Pacific* **125**, 1031 (2013).
10. Gaia Collaboration. Gaia Data Release 2. Summary of the contents and survey properties. *Astron. Astrophys.* **616**, A1 (2018).
11. Santerne, A. et al. PASTIS: Bayesian extrasolar planet validation - II. Constraining exoplanet blend scenarios using spectroscopic diagnoses. *Mon. Not. R. Astron. Soc.* **451**, 2337–2351 (2015).
12. Bodenheimer, P., Stevenson, D. J., Lissauer, J. J. & D'Angelo, G. New formation models for the Kepler-36 system. *Astrophys. J.* **868**, 138 (2018).
13. Dorn, C. et al. A generalized Bayesian inference method for constraining the interiors of super Earths and sub-Neptunes. *Astron. Astrophys.* **597**, A37 (2017).
14. Mizuno, H., Nakazawa, K. & Hayashi, C. Instability of a gaseous envelope surrounding a planetary core and formation of giant planets. *Prog. Theor. Phys.* **60**, 699–710 (1978).
15. Rafikov, R. R. Atmospheres of protoplanetary cores: critical mass for nucleated instability. *Astrophys. J.* **648**, 666–682 (2006).
16. Piso, A.-M. A., Youdin, A. N. & Murray-Clay, R. A. Minimum core masses for giant planet formation with realistic equations of state and opacities. *Astrophys. J.* **800**, 82 (2015).
17. Stassun, K. G., Collins, K. A. & Gaudi, B. S. Accurate empirical radii and masses of planets and their host stars with gaia parallaxes. *Astron. J.* **153**, 136 (2017).
18. Fortney, J. J., Saumon, D., Marley, M. S., Lodders, K. & Freedman, R. S. Atmosphere, interior, and evolution of the metal-rich transiting planet HD 149026b. *Astrophys. J.* **642**, 495–504 (2006).
19. Ikoma, M., Guillot, T., Genda, H., Tanigawa, T. & Ida, S. On the origin of HD 149026b. *Astrophys. J.* **650**, 1150–1159 (2006).
20. Delrez, L. et al. WASP-121 b: a hot Jupiter close to tidal disruption transiting an active F star. *Mon. Not. R. Astron. Soc.* **458**, 4025–4043 (2016).
21. Collier Cameron, A. & Jardine, M. Hierarchical Bayesian calibration of tidal orbit decay rates among hot Jupiters. *Mon. Not. R. Astron. Soc.* **476**, 2542–2555 (2018).
22. Hamer, J. H. & Schlaufman, K. C. Hot Jupiters are destroyed by tides while their host stars are on the main sequence. *Astron. J.* **158**, 190 (2019).
23. Winn, J. N. et al. Absence of a metallicity effect for ultra-short-period planets. *Astron. J.* **154**, 60 (2017).
24. Iaroslavitz, E. & Podolak, M. Atmospheric mass deposition by captured planetesimals. *Icarus* **187**, 600–610 (2007).
25. Brouwers, M. G., Vazan, A. & Ormel, C. W. How cores grow by pebble accretion. I. Direct core growth. *Astron. Astrophys.* **611**, A65 (2018).
26. Mordasini, C. in *Handbook of Exoplanets* (ed. Pudritz, R.) 2425–2474 (Springer, 2018).
27. Crida, A., Morbidelli, A. & Masset, F. On the width and shape of gaps in protoplanetary disks. *Icarus* **181**, 587–604 (2006).
28. Duffell, P. C. & MacFadyen, A. I. Gap opening by extremely low-mass planets in a viscous disk. *Astrophys. J.* **769**, 41 (2013).
29. Triaud, A. H. M. J. in *Handbook of Exoplanets* (eds Deeg, H. & Belmonte, J.) 1375–1401 (Springer, 2018).
30. Xie, J.-W. Transit timing variation of near-resonance planetary pairs. II. Confirmation of 30 planets in 15 multiple-planet systems. *Astrophys. J. Suppl. Ser.* **210**, 25 (2014).
31. Zeng, L. & Sasselov, D. A detailed model grid for solid planets from 0.1 through 100 Earth masses. *Publ. Astron. Soc. Pacif.* **125**, 227 (2013).

David J. Armstrong[1,2]✉, Théo A. Lopez[3], Vardan Adibekyan[4], Richard A. Booth[5], Edward M. Bryant[1,2], Karen A. Collins[6], Magali Deleuil[3], Alexandre Emsenhuber[7,8], Chelsea X. Huang[9], George W. King[1,2], Jorge Lillo-Box[10], Jack J. Lissauer[11], Elisabeth Matthews[9], Olivier Mousis[3], Louise D. Nielsen[12], Hugh Osborn[3], Jon Otegi[12,13], Nuno C. Santos[4,14], Sérgio G. Sousa[4], Keivan G. Stassun[15,16], Dimitri Veras[1,2], Carl Ziegler[17], Jack S. Acton[18], Jose M. Almenara[19], David R. Anderson[1,2], David Barrado[10], Susana C. C. Barros[4], Daniel Bayliss[1,2], Claudia Belardi[18], Francois Bouchy[12], César Briceño[20], Matteo Brogi[1,2,21], David J. A. Brown[1,2], Matthew R. Burleigh[18], Sarah L. Casewell[18], Alexander Chaushev[22], David R. Ciardi[23], Kevin I. Collins[24], Knicole D. Colón[25], Benjamin F. Cooke[1,2], Ian J. M. Crossfield[9], Rodrigo F. Díaz[26,27,28], Elisa Delgado Mena[4], Olivier D. S. Demangeon[4], Caroline Dorn[13], Xavier Dumusque[12], Philipp Eigmüller[29], Michael Fausnaugh[9], Pedro Figueira[4,30], Tianjun Gan[31], Siddharth Gandhi[2], Samuel Gill[1,2], Erica J. Gonzales[32], Michael R. Goad[18], Maximilian N. Günther[9], Ravit Helled[13], Saeed Hojjatpanah[4,14], Steve B. Howell[11], James Jackman[1,2], James S. Jenkins[33,34], Jon M. Jenkins[11], Eric L. N. Jensen[35], Grant M. Kennedy[1,2], David W. Latham[36], Nicholas Law[37], Monika Lendl[12,38], Michael Lozovsky[13], Andrew W. Mann[37], Maximiliano Moyano[39], James McCormac[1,2], Farzana Meru[1,2], Christoph Mordasini[8], Ares Osborn[1,2], Don Pollacco[1,2], Didier Queloz[40], Liam Raynard[18], George R. Ricker[9], Pamela Rowden[41], Alexandre Santerne[3], Joshua E. Schlieder[25], Sara Seager[9,42,43], Lizhou Sha[9], Thiam-Guan Tan[44], Rosanna H. Tilbrook[18], Eric Ting[11], Stéphane Udry[12], Roland Vanderspek[9], Christopher A. Watson[45], Richard G. West[1,2], Paul A. Wilson[1,2], Joshua N. Winn[46], Peter Wheatley[1,2], Jesus Noel Villasenor[9], Jose I. Vines[33] & Zhuchang Zhan[42]

[1]Centre for Exoplanets and Habitability, University of Warwick, Coventry, UK. [2]Department of Physics, University of Warwick, Coventry, UK. [3]Aix-Marseille Université, CNRS, CNES, LAM, Marseilles, France. [4]Instituto de Astrofísica e Ciências do Espaço, Universidade do Porto, CAUP, Porto, Portugal. [5]Institute of Astronomy, University of Cambridge, Cambridge, UK. [6]Center for Astrophysics, Harvard and Smithsonian, Cambridge, MA, USA. [7]Lunar and Planetary Laboratory, University of Arizona, Tucson, AZ, USA. [8]Physikalisches Institut, University of Bern, Bern, Switzerland. [9]Department of Physics and Kavli Institute for Astrophysics and Space Research, Massachusetts Institute of Technology, Cambridge, MA, USA. [10]Departamento de Astrofísica, Centro de Astrobiología (CSIC-INTA), Madrid, Spain. [11]NASA Ames Research Center, Moffett Field, CA, USA. [12]Observatoire Astronomique de l'Université de Genéve, Versoix, Switzerland. [13]Institute for Computational Science, University of Zurich, Zurich, Switzerland. [14]Departamento de Física e Astronomia, Faculdade de Ciências, Universidade do Porto, Porto, Portugal. [15]Department of Physics and Astronomy, Vanderbilt University, Nashville, TN, USA. [16]Department of Physics, Fisk University, Nashville, TN, USA. [17]Dunlap Institute for Astronomy and Astrophysics, University of Toronto, Toronto, Ontario, Canada. [18]School of Physics and Astronomy, University of Leicester, Leicester, UK. [19]Université Grenoble Alpes, CNRS, IPAG, Grenoble, France. [20]Cerro Tololo Inter-American Observatory, La Serena, Chile. [21]INAF Osservatorio Astrofisico di Torino, Pino Torinese, Italy. [22]Center for Astronomy and Astrophysics, TU Berlin, Berlin, Germany. [23]Caltech/IPAC-NASA Exoplanet Science Institute, Pasadena, CA, USA. [24]George Mason University, Fairfax, VA, USA. [25]NASA Goddard Space Flight Center, Exoplanets and Stellar Astrophysics Laboratory (Code 667), Greenbelt, MD, USA. [26]Facultad de Ciencias Exactas y Naturales, Universidad de Buenos Aires, Buenos Aires, Argentina. [27]Instituto de Astronomía y Física del Espacio (IAFE), CONICET – Universidad de Buenos Aires, Buenos Aires, Argentina. [28]International Center for Advanced Studies (ICAS) and ICIFI (CONICET), ECyT-UNSAM, Campus Miguelente, Buenos Aires, Argentina. [29]Institute of Planetary Research, German Aerospace Center, Berlin, Germany. [30]European Southern Observatory, Santiago, Chile. [31]Department of Astronomy and Tsinghua Centre for Astrophysics, Tsinghua University, Beijing, China. [32]Department of Astronomy and Astrophysics, University of California at Santa Cruz, Santa Cruz, CA, USA. [33]Departamento de Astronomía, Universidad de Chile, Santiago, Chile. [34]Centro de Astrofísica y Tecnologías Afines (CATA), Santiago, Chile. [35]Department of Physics and Astronomy, Swarthmore College, Swarthmore, PA, USA. [36]Harvard-Smithsonian Center for Astrophysics, Cambridge, MA, USA. [37]Department of Physics and Astronomy, University of North Carolina at Chapel Hill, Chapel Hill, NC, USA. [38]Space Research Institute, Austrian Academy of Sciences, Graz, Austria. [39]Instituto de Astronomía, Universidad Católica del Norte, Antofagasta, Chile. [40]Cavendish Laboratory, University of Cambridge, Cambridge, UK. [41]School of Physical Sciences, The Open University, Milton Keynes, UK. [42]Department of Earth, Atmospheric and Planetary Sciences, Massachusetts Institute of Technology, Cambridge, MA, USA. [43]Department of Aeronautics and Astronautics, Massachusetts Institute of Technology, Cambridge, MA, USA. [44]Perth Exoplanet Survey Telescope, Perth, Western Australia, Australia. [45]Astrophysics Research Centre, Queen's University Belfast, Belfast, UK. [46]Department of Astrophysical Sciences, Princeton University, Princeton, NJ, USA. ✉e-mail: d.j.armstrong@warwick.ac.uk

Methods

Observations and analysis

TESS. TOI-849 was observed in TESS (Transiting Exoplanet Survey Satellite) sector 3 (20 September 2018 to 18 October 2018), Camera 2 and CCD 3, with 30-min cadence on the full-frame images (FFIs). The calibrated FFIs, available at the Michulski Archive for Space Telescopes (MAST; https://archive.stsci.edu/missions-and-data/transiting-exoplanet-survey-satellite-tess), were produced by the TESS Science Processing Operations Center (SPOC)[32]. The candidate was detected by the MIT Quick Look pipeline[33] with a signal-to-noise ratio of 18. It exhibited consistent transit depth in the multi-aperture analysis and appeared to be on target in the difference image analysis. It passed all the vetting criteria set by the TESS Science Office and was released as a TESS Object of Interest.

The aperture showing minimal scatter was found to be circular with a radius of 2.5 pixels, and the background was determined on an annulus with a width of 3 pixels and an inner radius of 4 pixels. We rejected outliers due to spacecraft momentum dump with the quaternion time series provided by the spacecraft data. Further long-timescale trends were removed using a B-spline-based algorithm[34]. No evidence of photometric activity was observed. The light curve was further detrended to remove residual long-term trends using a modified Savitzky–Golay filter[35], whereby a sliding window was used to fit a three-dimensional polynomial function to the data while ignoring outliers. Both flattening operations were carried out ignoring in-transit data points. Data before 2,458,383.78 BJD and after 2,458,405.77 BJD were masked because during that time the TESS operations team carried out several experiments on the attitude control system, causing the jitter profile to differ from normal. Data points between 2,458,394.54 BJD and 2,458,397.0 BJD were masked because of scattered light. The resulting light curve is shown in Fig. 1.

NGTS. Two full transits of TOI-849 were observed on the nights of 8 August 2019 and 11 August 2019 UT (universal time) using the Next Generation Transit Survey (NGTS)[8] at the Paranal Observatory of the European Southern Observatory (ESO) in Chile, which are plotted in Fig. 1. The NGTS facility consists of 12 fully robotic 20-cm telescopes coupled to Andor iKon-L 936 cameras, each with an instantaneous field of view of 8 square degrees and a pixel scale of 5″ per pixel. On both nights, ten NGTS telescopes were used to simultaneously observe the transit. Becauise the photometric noise was found to be uncorrelated between the individual NGTS telescopes, we can combine the light curves to achieve ultrahigh precision photometry for TOI-849. A total of 29,654 images were obtained with an exposure time of 10 s using the custom NGTS filter (520–890 nm). The observations were all obtained at an airmass of $z < 2$ and with photometric observing conditions. The telescope guiding was performed using the DONUTS auto-guiding algorithm[36], which provides sub-pixel-level stability of the target position on the charge-coupled device (CCD). We did not require the use of flat fields during the image reduction, because of the high precision of the auto-guiding. This reduction was performed using a custom aperture photometry pipeline, in which the 100 best comparison stars were selected and ranked on the basis of their proximity to the target star in the parameters of on-sky separation, apparent magnitude and colour. This large number of optimized comparison stars ccould be obtained because of the wide field of view of the NGTS telescopes, and again improved the precision of the NGTS light curves by reducing the presence of correlated noise.

HARPS. We obtained radial velocity (RV) measurements of TOI-849 with the High Accuracy Radial velocity Planet Searcher (HARPS) spectrograph (resolving power $R = 115{,}000$) mounted on the 3.6-m telescope at ESO's La Silla Observatory[37]. Thirty three observations were taken between 28 July 2019 and 28 December 2019 in HAM mode, as part of the NCORES large programme (ID 1102.C-0249). An exposure time of at least 1,200 s was used, giving a signal-to-noise ratio of ~20 per pixel. Typically, the star was observed 2–3 times per night. The data were reduced with the offline data reduction software HARPS pipeline. RV measurements were performed using a weighted cross-correlation function (CCF) method with a G2V template[38,39]. The line bisector (BIS) and the full-width at half-maximum (FWHM) were measured using published methods[40]. No correlation was seen between the RVs and the calculated BIS, FWHM, or CCF contrast ($R < 0.09$ in all cases). The RV measurements are listed in Extended Data Table 4, and the RV data, photometry and best fit are shown in Fig. 1. A jitter of 4.2 m s^{-1} was seen, consistent with the low photometric activity level. The BIS and FWHM are shown in Extended Data Fig. 2. We investigated the CCFs for contributions from unresolved stellar companions by removing Gaussian fits to the individual CCF profiles and studying the residuals (Extended Data Fig. 3). No evidence of additional companions was seen. Finally, we studied the RV residuals and found no evidence of further periodicity, as shown in Extended Data Fig. 3.

LCOGT and PEST. Two full transits of TOI-849 were observed on the nights of 30 July 2019 and 9 August 2019 UT in the i′ band using exposure times of 30 s and 40 s, respectively. Data were taken for an additional night on 14 July 2019 UT, which unfortunately missed the transit relative to the revised ephemeris from our joint fit. The data with the transits are plotted in Extended Data Fig. 1. Both observations used the CTIO node of the Las Cumbres Observatory Global Telescope (LCOGT) 1-m network[9]. We used the TESS Transit Finder, which is a customized version of the Tapir software package[41], to schedule our transit observations. The telescopes are equipped with 4,096 × 4,096 LCO SINISTRO cameras having an image scale of 0.389″ per pixel, resulting in a 26′ × 26′ field of view. The images were calibrated using the standard LCOGT BANZAI pipeline, and the photometric data were extracted using the AstroImageJ software package[42]. The first full transit on 30 July was observed with the telescope in focus and achieved a point spread function FWHM of ~1.6″. Circular apertures with radius 3.1″ were used to extract differential photometry for the target star and for all stars within 2.5′ that were brighter than TESS band magnitude 19. All of the neighbouring stars were excluded as possible sources of the TESS detection, and the event was detected on target. A circular aperture with radius 8″ was used for the other LCOGT observation, which was slightly defocused to an FWHM of ~4″. The nearest star in the Gaia Data Release 2 catalogue is 39″ to the north of TOI-849, so the target star photometric apertures were uncontaminated by known nearby stars.

A full transit was observed on 20 August 2019 UT in the R_c band from the Perth Exoplanet Survey Telescope (PEST) near Perth, Australia. The 0.3-m telescope is equipped with a 1,530 × 1,020 SBIG ST-8XME camera with an image scale of 1.2″ per pixel, resulting in a 31′ × 21′ field of view. Systematics at the level of the shallow transit depth precluded inclusion of these data in the joint fit.

NACO/VLT. TOI-849 was imaged with the NAOS/CONICA instrument onboard the Very Large Telescope (NACO/VLT) on the night of 14 August 2019 in NGS mode with the Ks filter. We took nine frames with an integration time of 17 s each, and dithered between each frame. We performed a standard reduction using a custom IDL pipeline: we subtracted flats and constructed a sky background from the dithered science frames, aligned and co-added the images, and then injected fake companions to determine a 5σ detection threshold as a function of radius. We obtained a contrast of 5.6 magnitudes at 1″, and no companions were detected. The contrast curve is shown in Extended Data Fig. 4.

SOAR. We searched for nearby sources to TOI-849 with SOAR (Southern Astrophysical Research) speckle imaging[43,44] on 12 August 2019 UT, observing in a similar visible bandpass as TESS. We detected no nearby sources within 3″of TOI-849. The 5σ detection sensitivity and

the speckle auto-correlation function from the SOAR observation are plotted in Extended Data Fig. 4.

AstraLux. We obtained a high-spatial-resolution image of TOI-849 with the AstraLux camera[45], which is installed at the 2.2-m telescope of Calar Alto Observatory (Almería, Spain), using the 'lucky imaging' technique[46]. We obtained 24,400 images in the SDSSz band with 20 ms exposure time, well below the coherence time. The CCD was windowed to match 6″ × 6″. We used the observatory pipeline to perform basic reduction of the images and subsequent selection of the best-quality frames. This was done by measuring their Strehl ratio[47] and selecting only the 10% with the highest value of this parameter (an effective integration time of 48 s). Then, these images were aligned and combined to obtain the final high-spatial-resolution image. We estimated the sensitivity curve of this high-spatial-resolution image[48,49] based on the injection of artificial stars in the image at different angular separations and position angles and by measuring the retrieved stars using the detection algorithms used to look for real companions. No companions were detected in this image within the sensitivity limits. Both the high-resolution image and the contrast curve are shown in Extended Data Fig. 4.

Zorro/Gemini South. TOI-849 was observed on 13 September 2019 UT using the Zorro speckle instrument on the Gemini South telescope. Zorro provides simultaneous speckle imaging in two bands, 562 nm and 832 nm, with output data products including a reconstructed image and with robust limits on companion detections[50]. Extended Data Fig. 4 shows our 562-nm contrast curve from which we find that TOI-849 is a single star with no companion brighter than about 5 magnitudes detected within 1.75″.

Spectroscopic analysis and chemical abundances. The spectroscopic analysis used to derive the effective temperature ($T_{\rm eff}$), surface gravity (log$g$), microturbulence ($\xi_{\rm t}$) and metallicity ([Fe/H]) and the respective errors follows previous work[51,52]. Equivalent widths are measured for a list of well defined iron lines. We use the combined HARPS spectrum of TOI-849 and ARES v2 code[53,54] to measure the equivalent widths. In the spectral analysis we look for the ionization and excitation equilibrium. The process makes use of a grid of Kurucz model atmospheres[55] and the radiative-transfer code MOOG[56]. The resulting values are $T_{\rm eff}$ = 5,329 ± 48 K, log$g$ = 4.28 ± 0.09, $\xi_{\rm t}$ = 0.82 ± 0.08 and [Fe/H] = 0.20 ± 0.03.

The same tools and models are also used to derive stellar abundances for several chemical elements. For this, we use the classical curve-of-growth analysis method assuming local thermodynamic equilibrium. Although the equivalent widths of the spectral lines are automatically measured with ARES, for elements with only two to three lines available we perform careful visual inspection of the equivalent width measurements. Chemical abundances are derived by closely following past work[57]. The final abundances derived are [Na I/H] = 0.30 ± 0.16, [Mg I/H] = 0.24 ± 0.06, [Al I/H] = 0.30 ± 0.06, [Si I/H] = 0.24 ± 0.08, [Ca I/H] = 0.16 ± 0.07, [Sc II/H] = 0.23 ± 0.09, [Ti I/H] = 0.25 ± 0.09, [Cr I/H] = 0.23 ± 0.07 and [Ni I/H] = 0.28 ± 0.04.

Extended Data Figure 5 shows a comparison of the abundances of TOI-849 with those found in solar-neighbourhood stars[58] of similar atmospheric parameters. In terms of chemical composition, TOI-849 seems to be very similar to the solar-neighbourhood stars, showing a slight enhancement in the iron-peak elements Cr and Ni.

Joint RV and photometric fit. The HARPS RVs, the TESS, NGTS and LCOGT photometry, and the spectral energy distribution (SED) were jointly analysed in a Bayesian framework, using the PASTIS software[11,59]. For the SED, we used the visible magnitudes from the American Association of Variable Star Observers Photometric All-Sky Survey (APASS) and the near-infrared magnitudes from the Two-Micron All-Sky Survey (2MASS) and the Wide-field Infrared Survey Explorer (AllWISE)[60–62]. The RVs were fitted using a Keplerian orbit model and a linear drift. The light curves were modelled with the JKT Eclipsing Binary Orbit Program[63] using an oversampling factor of 180, 12, 6 and 7 for the TESS and the three LCOGT-CTIO light curves, respectively. The NGTS light curves were not oversampled because the integration of the individual data is short with respect to the transit duration[64]. Finally, the SED was modelled using the BT-Settl library of stellar atmosphere models[65]. The system parameters and associated uncertainties were derived using the Markov chain Monte Carlo (MCMC) method implemented in PASTIS. The stellar parameters were computed using the Dartmouth evolution tracks[66] at each step of the chains, accounting for the asterodensity profiling[67]. We also used the PARSEC evolution tracks, with consistent results.

Regarding the priors, we used a normal distribution with median and width from the spectral analysis to obtain the stellar temperature, surface gravity and iron abundance. For the systemic distance to Earth, we used a normal prior centred on the Gaia Data Release 2 value[10], taking into account the distance bias correction[68]. For the orbital period and transit epoch, we used normal priors centred on first-guess values from an independent analysis of the NGTS and TESS light curves alone, to improve the convergence of the MCMCs. For the orbital inclination we used a sine prior and for the eccentricity a truncated normal prior with width 0.083 (ref. [69]). For the other parameters, we used uniform priors with width large enough to not artificially decrease the uncertainties. Initial fits gave an eccentricity of 0.036 ± 0.027 (1σ error; result indistinguishable from zero), so we fixed the eccentricity to zero for the final fitting. A linear drift was included for the HARPS data that was also indistinguishable from zero and did not affect the results. Further testing with a quadratic drift model showed no changes in the fit parameters and was dropped.

We ran 20 MCMCs with 2×10^5 iterations. We checked the convergence with a Kolmogorov–Smirnov test[11,59], removed the burn-in phase and merged the remaining chains. The limb-darkening coefficients were computed using previously computed stellar parameters and tables[70]. Finally, the physical parameters and associated uncertainties were derived from samples from the merged chain. The results for the Dartmouth and PARSEC evolution tracks are shown in Extended Data Tables 1, 2. The fit transit depth implies a joint signal-to-noise ratio of 386 (ref. [59]) for the transit.

As an independent check on the derived stellar parameters, we performed an analysis of the broadband SED together with the Gaia parallax to determine an empirical value of the stellar radius[17,71,72]. We pulled the $B_{\rm T}V_{\rm T}$ magnitudes from Tycho-2, the BVgri magnitudes from APASS, the $JHK_{\rm S}$ magnitudes from 2MASS, the $W1$–$W4$ magnitudes from WISE and the G magnitude from Gaia. Together, the available photometry spans the full stellar SED over the wavelength range 0.4–22 μm. We also checked the GALEX near-ultraviolet flux, which was not used in the fit, because it suggests a modest level of chromospheric activity.

We performed the independent fit using the Kurucz stellar atmosphere models, with priors on $T_{\rm eff}$, log$g$ and [Fe/H] from the spectroscopic values. The remaining free parameter is the extinction (A_V), which we limited to the maximum line-of-sight extinction from known dust maps[73]. The resulting fit has a reduced χ^2 of 4.5 and a best-fit extinction of A_V = 0.04 ± 0.03. Integrating the (unextincted) model SED gives a bolometric flux at Earth of $F_{\rm bol} = 3.713 \pm 0.086 \times 10^{-10}$ erg s cm^{-2}. Taking $F_{\rm bol}$ and $T_{\rm eff}$ together with the Gaia parallax, adjusted by +0.08 mas to account for a previously reported systematic offset[74], gives the stellar radius as $R = (0.896 \pm 0.020) R_{\odot}$. Finally, estimating the stellar mass from known empirical relations[75], assuming solar metallicity, gives $M = (1.01 \pm 0.08) M_{\odot}$, which, combined with the radius, gives a mean stellar density of $\rho = 1.99 \pm 0.19$ g cm^{-3}. These values are consistent with the stellar parameters found from the PASTIS MCMC chain, so we adopt the PASTIS values for our results.

Interpretation and discussion

Interior-structure characterization. Given the mass and radius of TOI-849b, it is clear that the planet does not represent a larger version of Neptune. This is demonstrated in Fig. 2, which shows the mass–radius relation for a pure-water curve and a planet consisting of 95% water and 5% H–He atmosphere, corresponding to a stellar irradiation of $F/F_{\oplus}$ = 3,000 (TOI-849b). TOI-849b sits on the pure-water curve and well below the 5% strongly irradiated curve, suggesting that the H–He mass fraction is of the order of only a few per cent, if not negligible. Figure 3 also shows that TOI-849b is relatively isolated in parameter space, suggesting that it is somewhat unique and could have been subjected to an unusually aggressive removal of the primordial H–He envelope.

We explore layered-structure models containing variable fractions of the H–He envelope. Typical available models are not suited to this planet owing to the high pressures in the interior, requiring exotic equations of state. Further, for planets this massive, the interior layers are probably not as distinct as for smaller planets, with composition gradients more likely[12]. Rather than build a full model of the interior, which would not be valid for the reasons stated, we consider some illuminating limiting cases.

We model the planetary interior of TOI-849b assuming a pure iron core, a silicate mantle, a pure water layer, and a H–He atmosphere. We build a structure model based on previous work[13] except for the iron core, for which we use an updated equation of state[76]. For the silicate mantle, the equilibrium mineralogy and density are computed as a function of pressure, temperature and bulk composition by minimizing the Gibbs free energy[77]. For the water, we use a quotidian equation of state[78] for low pressures and a previously tabulated equation of state[79] for pressures above 44.3 GPa. For H–He, we assume a proto-solar composition[80]. We then solve the standard structure equations.

We then estimate the possible range of the H–He mass fraction in TOI-849b that fits the derived mass and radius. To estimate the maximum possible mass of an H–He envelope, we assume a planet without water. The core-to-mantle fraction is set by the stellar abundance [Fe/Si] of the host star[81]. The minimum H–He mass fraction is estimated by assuming a large fraction of water of 70% by mass, which corresponds to a water-rich planet. We search for the maximum and minimum H–He mass fractions for a grid of planetary masses and radii covering the observed values and their 2σ error range. It is found that that H–He mass fraction is at minimum $2.9^{+0.8}_{-1.0}$% and at maximum $3.9^{+0.8}_{-0.9}$%, suggesting that the heavy-element mass is greater than $38M_{\oplus}$. It should be noted that our models assume a pure H–He atmosphere, whereas in reality the atmosphere is expected to include heavier elements, as inferred by recent formation models[82]. This is particularly true for planets this massive, where the interior layers are probably not as distinct as for smaller planets. The existence of heavy elements in the H–He atmosphere would lead to compression, and can therefore increase the planetary H–He mass fraction. However, for the case of TOI-849b, the difference is expected to be very moderate because the planet mass is clearly dominated by heavy elements. Previous work calculated the effect of varying atmospheric water content on planetary radii for fixed masses and H–He gas mass fractions[83]. Applying that model to TOI-849b shows that the inferred planet radius is only affected on the level of a few per cent for atmospheric water content ranging from 0 to 70%. As such, we expect the plausible increase in H–He to be small even for high levels of volatile enrichment in the planetary envelope. We can therefore conclude that the mass fraction of H–He is at most a few per cent.

Photoevaporation rate. We explored the X-ray and extreme ultraviolet irradiation of the planet—the wavelengths most relevant for atmospheric mass loss[84]. Archival X-ray data exist for the system only from the ROSAT all-sky survey, where the nearest detected source is an arcminute away, too far to be associated with TOI-849. Instead, we applied known empirical relations linking X-ray emission with age[85], estimating $L_X/L_{bol} = 7.5 \times 10^{-7}$ at the current age, where L_X is the X-ray luminosity and L_{bol} the bolometric luminosity. This figure implies an X-ray flux at Earth of 3.0×10^{-16} erg s^{-1} cm^{-2}, much too faint to be visible with XMM-Newton or Chandra. We extrapolated our X-ray estimate to the unobservable extreme ultraviolet band using previously derived relations[86,87].

To estimate mass-loss rates, we applied both the energy-limited approach[88,89], and a method based on interpolating and approximating to hydrodynamical simulations[90,91]. The latter yields a loss rate of 1.8×10^{11} g s^{-1}, more than an order of magnitude larger than the former when assuming a canonical efficiency of 15%. By integrating over the planet's extreme ultraviolet history, and starting at a Jupiter mass and radius, we estimate total lifetime losses of 4.0% and 0.81% of the planet's mass using the energy-limited and Kubyshkina methods, respectively. Although these calculations have the limitation of assuming a constant radius across the lifetime, these losses are not enough to evolve the planet to one slightly smaller than Neptune, so we can be sure that the planet did not start as a Jupiter-like giant if its evolution has been solely through photoevaporation.

An intermediate starting point is the planet HD149026b[3], a giant planet with mass $(121 \pm 19)M_{\oplus}$ and radius $(8.3 \pm 0.2)R_{\oplus}$ (ref. [17]). For this planet, we estimate total lifetime losses of 11.42% and 100% of the planet's mass using the energy-limited and Kubyshkina methods, respectively. These are likely to be overestimates owing to the constant-radius assumption, which clearly becomes flawed after mass loss representing a large fraction of the planet's mass. As such, finding the limits of photoevaporation in creating a planet like TOI-849b requires detailed models beyond the scope of this paper.

Co-orbital bodies and exomoons. The anomalously large density found for planet TOI-849b allows us to explore alternative scenarios for the origin of this signal. One of the most relevant ones is the co-orbital case. Although these configurations have not yet been confirmed in any extrasolar systems despite several efforts[92–96], some candidates have arisen from studies such as Kepler-91[97] or the recent TOI-178[98]. Indeed, an additional planet in the system with the same orbital period as that of TOI-849b but not transiting owing to a mutual inclination between their orbits (or that is too small to be detected by TESS) could explain the large mass measured for such a small planet radius.

We here explore the scenario in which two planetary-mass bodies share the same orbital period in a 1:1 mean-motion resonance configuration. In such a case, the mass that we measure in the joint fit would be distributed in two planetary-mass objects. Such configurations are allowed by dynamical stability studies, which demonstrate that the only condition for the stability of co-orbital configurations is that the total mass of the planet plus its co-orbital companion must be smaller than 3.8% of the mass of the star[99]. Regardless of the formation process, and given the mass of the star and the estimated mass of TOI-849b, the co-orbital scenario would be stable for any planetary mass of the accompanying body.

To test this hypothesis, we apply a recently derived procedure to analyse the RV of the star using a new RV equation including two Keplerian components[95,96,100]. The new equation can be simplified so that only one extra parameter, α, is included[100]. This parameter depends on the trojan-to-planet mass ratio, so that if positive (negative), a trojan candidate might be in L_5 (L_4). For this analysis, we first assume a circular orbit, thus having five parameters: namely, the RV semi-amplitude K_{coorb}, the orbital period, the main-planet time of conjunction $T_{0,b}$, the systemic velocity γ and the alpha parameter α. We use Gaussian priors on the orbital period and time of conjunction with the parameters derived from the one-planet analysis (see Extended Data Table 1) and uniform priors for the alpha parameter $\mathcal{U}(-1, 1)$ km s^{-1} and systemic velocity $\mathcal{U}(9.1, 9.5)$ km s^{-1}. We also include a jitter term and a slope.

We use *emcee*[101] with 50 walkers and 5,000 steps per walker to explore the parameter space. We use the last half of each chain to compute the final posterior distributions. For the key parameter α, we obtain $\alpha = -0.092^{+0.060}_{-0.064}$. This value is 1.5σ away from zero and hence compatible with it within a 95% confidence level. The posterior distribution allows us to discard co-orbitals more massive than $8M_\oplus$ at the 95% confidence level assuming a mean resonant angle ζ, where $\zeta = \lambda_1 - \lambda_2$ and λ_i is the mean longitude of each of the two co-orbitals, of 60°. In practice, this assumes that the trojan planet would have been located exactly at the Lagrangian point during the timespan of the observations. In such a case, the transiting planet would have a mass of $31M_\oplus$, still uniquely high for its radius. A particular arrangement of trojan planets whereby equal-mass trojans are present in both the L_4 and L_5 Lagrangian points could in principle mimic the observed HARPS data. Such a scenario is observationally indistinguishable from the single-planet model while being notably more complex, and we reject it on that basis.

A related hypothesis is that of a 'double planet' or moon with non-negligible mass. In such a scenario, there is no distinguishable effect on the RVs and hence the apparent large mass would be split over additional bodies. We estimate the minimum stable satellite density by considering where the Hill radius and Roche limit of the planet overlap for TOI-849b[102]. Equation (5) of ref. [102] gives a minimum stable satellite density of 38 g cm^{-3}, much denser than pure iron. As such, we conclude that physically realistic exomoons are unstable around TOI-849b and this hypothesis can be discarded.

Planet population synthesis models. We explored possible formation channels for such dense Neptune-sized planets using the Bern Generation 3 Model of Planetary Formation and Evolution, which is an update on the currently published version[26]. The main changes in the model are reflected in the following description. The model self-consistently evolves a one-dimensional gas disk, the dynamical state of the solids, the accretion of solids and gas by the protoplanets, their interiors, and their dynamical evolution by gravitational interactions and gas-driven migration.

For the gas disk, the model computes a one-dimensional radial profile that is evolving viscously[103], with the macroscopic viscosity given by the standard α parameterization[104]. The vertical structure is now computed using a vertically integrated approach[105] that includes the effect of stellar irradiation[106]. Stellar parameters are retrieved from known evolution tracks[107]. We include additional sink terms for the accretion by the planets, as well as both internal[108] and external[109] photoevaporation.

The model assumes that planetesimals accrete in the oligarchic regime[110–112], and their capture cross-section is computed consistently with the envelope structure[113]. The internal structure equations[114] are solved for the gas envelope. In the initial (or 'attached') phase, the envelope is in equilibrium with the surrounding disk, and the internal structure is used to determine the gas mass. Gas accretion is governed by the ability of the planet to radiate away the gravitational energy released from the accretion of both solids and gas[115,116]. When the accretion rate exceeds the supply from the disk, the envelope is no longer in equilibrium with the disk and contracts[117]. In this 'detached' phase, the internal structure is used to retrieve the planet's radius and luminosity.

Dynamical interactions between the planets are simulated by means of the Mercury *N*-body integrator[118]. After a giant impact, an additional luminosity is included[119] to determine whether the gas envelope is ejected. Gas-driven type I migration is computed in line with past work[120], accounting for how local thermodynamic effects in the disk[121] and planet eccentricities and inclinations[122] affect the corotation torques. Type II migration and the switch between the two migration regimes are computed in line with past work[123]. Torques and damping are included in the *N*-body calculation by means of additional forces.

The formation stage lasts for 20 Myr. The model then transitions into the evolution stage, in which the planets are followed individually for up to 10 Gyr. This stage includes thermodynamical evolution of the envelope, atmospheric escape[124,125] and tidal migration[126] with a fixed stellar dissipation parameter of $Q_\star = 10^6$.

To obtain a synthetic population, we update a previously published procedure[127]. We use the literature disk mass distribution[128], and the characteristic radius, which determines the radial distribution of the gas, is obtained following a known relationship[129]. The location of the inner edge of the disk has a log-normal distribution in period with a mean of 4.7 d (ref. [130]). The dust-to-gas ratio is obtained from the observed stellar [Fe/H] (ref. [127]), but using the primordial solar metallicity as a reference[131]. The initial surface density profile of solids has a steeper slope than that of the gas[132], leading to a higher concentration in the inner region. In each disk, 20 lunar-mass ($10^{-2}M_\oplus$) planetary embryos are emplaced at the beginning. Their initial positions are randomly selected between the inner edge of the disk up to 40 AU, with a uniform probability in the logarithm of the semi-major axis.

In those models, which were run before the discovery of TOI-849b, we found three planets that exhibit similar mass, radius and eccentricity to TOI-849b out of a total sample of 1,000. These planets have masses between $20M_\oplus$ and $50M_\oplus$ and have an ice content of 20–30% by mass, but no H/He. They started as embryos outside the ice line and migrated steadily to a position close to the inner edge of the disk. The removal of the primordial H/He is due to one or two giant impacts that took place at the end of the migration, which means that the planets were unable to accrete a second H/He envelope. For one of the three planets only a single impact is seen, whereas two impacts occur in the others. In all cases, only a single impact is needed to remove the envelope. To place this in context, 70% of close-in Neptunes in the simulations, defined as having a semi-major axis <0.04 AU, had at least one impact with a body of mass $>1M_\oplus$ during their formation. As such, impacts are not particularly rare, but the timing of the impact at the end of the migration phase is what prevents reaccretion and leads to a permanently lost envelope.

Owing to the high equilibrium temperature, it is likely that the remaining ices evaporate to form a secondary atmosphere consisting of water and possibly other volatiles like CO and CO_2. Such an envelope leads to radii comparable to that of the discovered planet. From the modelling point of view, the population synthesis models prefer planets with small envelopes consisting entirely of ices. The evolution tracks of the three considered model planets are shown in Extended Data Fig. 6.

Although no model planets similar to TOI-849b were found from other formation pathways, this should not be taken as evidence against other hypotheses, such as gap opening limiting the accretion, or tidal disruption. The Bern models do not include gap opening in the disk as a limiting factor in gas accretion and use simplified assumptions for tidal interactions[126] that do not include high-eccentricity migration.

Tidally induced thermalization events. The high bulk density of TOI-849b (5.2 g cm^{-3}) relative to that of Neptune (1.6 g cm^{-3}) suggests that the planet (with a radius equal to 90% of Neptune's) might currently represent the core of a previously giant planet. For this scenario to be viable, the planet needs to originate from a gas giant and to have expelled mass, possibly during orbit shrinkage and circularization. This evolutionary pathway may occur as a result of chaotic tides[133–135], where the planet's internal f-modes were excited after the planet was gravitationally scattered onto a highly eccentric orbit. Energy buildup in the modes could have then led to thermalization events, potentially ejecting atmospheric layers[136,137]. After the resulting core left the chaotic regime, subsequent orbital evolution over the ~9-Gyr main-sequence lifetime of the parent star may have proceeded with weakly dissipative equilibrium tides, leading to the current orbit. In this scenario, the planet may have expelled 1–2 orders of magnitude more mass than its current value.

Accumulation of the internal mode energy leads to thermalization events, which subsequently deposit energy into the planet's interior and reset the mode amplitude. Possible results of the thermalization events include inflation, mass ejection or both; TOI-849b could have

experienced such events and still retained some or all of its atmosphere. Although their trigger and consequences remain largely unknown, previous work has assumed that such events occur when the accumulated mode energy equals 10% of the planet's binding energy[136]

$$E_{\mathrm{bind}} \approx \frac{GM_{\mathrm{p}}^2}{R_{\mathrm{p}}}, \quad (1)$$

where M_{p} and R_{p} are the mass and radius of the planet, respectively, and G is the gravitational constant. That work[136] also demonstrated that the changes in orbital evolution resulting from the thermalization events are largely independent of this choice of 10%. With this selection, it has been illustrated that the number of thermalization events that a planet experiences is positively correlated with an increasing puffiness of the planet and a decreasing orbital pericentre[137]. It has been shown that even a dense gas giant with a pericentre of about $1.5R_{\odot}$ would experience at least one thermalization event, albeit with a smaller-mass central star. TOI-849b, which currently resides at a distance of about $3R_{\odot}$, previously would have harboured a pericentre that is just half of that value if angular momentum was conserved as its eccentricity decreased from almost unity to zero, under the high-eccentricity circularization scenario.

Atmospheric follow-up observations. Future observations of TOI-849b may attempt to identify its atmospheric composition. TOI-849b represents a new class of dense, high-mass planet and its atmosphere will provide a counterpoint to other planets of different type, as well as potentially allow the characterization of a non-H_2-rich atmosphere. Given the high equilibrium temperature of the planet, and hence the potential for evaporation of volatiles to form a secondary atmosphere, such observations may be able to detect core material in the atmosphere, and regardless will help to place TOI-849b in context against other Neptune-sized planets, other planets with or without high irradiation, the few planets inside the Neptunian desert and the bulk composition of the star. Such comparisons are the goal of the European Space Agency's Ariel mission[138], although the magnitude of TOI-849 will arguably require next-generation telescopes for atmospheric observations, such as the James Webb Space Telescope or the European Extremely Large Telescope.

Data availability

TESS data are publicly available at MAST (https://archive.stsci.edu/missions-and-data/transiting-exoplanet-survey-satellite-tess). The HARPS data used in this study are available within the paper or the Supplementary Information files and were collected under ESO programme ID 1102.C-0249. The NGTS (Data Tags 19249 and 19250), LCOGT (Data Tags 5106 and 5386) and specific detrended TESS light curve (Data Tag 19248) used in this work are available via the Exofop-TESS archive (https://exofop.ipac.caltech.edu/tess/).

Code availability

The PASTIS code has been published previously[11,59]. The latest version of the ARES code (ARES v2) is available at http://www.astro.up.pt/~sousasag/ares.

32. Jenkins, J. M. et al. The TESS science processing operations center. In *Proc. SPIE Software and Cyberinfrastructure for Astronomy IV Series*, Vol. 9913, 99133 (SPIE, 2016).
33. Huang, X. et al. A quick look into the first discoveries of TESS. In *American Astronomical Society Meeting Abstracts* Vol. 233, 209.08 (American Astronomical Society, 2019).
34. Vanderburg, A. & Johnson, J. A. A technique for extracting highly precise photometry for the two-wheeled Kepler mission. *Publ. Astron. Soc. Pacific* **126**, 948 (2014).
35. Armstrong, D. J. et al. K2 variable catalogue: variable stars and eclipsing binaries in K2 campaigns 1 and 0. *Astron. Astrophys.* **579**, A19 (2015).
36. McCormac, J. et al. DONUTS: a science frame autoguiding algorithm with sub-pixel precision, capable of guiding on defocused stars. *Publ. Astron. Soc. Pacific* **125**, 548 (2013).
37. Mayor, M. et al. Setting new standards with HARPS. *Messenger* **114**, 20–24 (2003).
38. Baranne, A. et al. ELODIE: a spectrograph for accurate radial velocity measurements. *Astron. Astrophys. Suppl. Ser.* **119**, 373–390 (1996).
39. Pepe, F. et al. HARPS: ESO's coming planet searcher. Chasing exoplanets with the La Silla 3.6-m telescope. *Messenger* **110**, 9–14 (2002).
40. Boisse, I. et al. Disentangling between stellar activity and planetary signals. *Astron. Astrophys.* **528**, A4 (2011).
41. Jensen, E. Tapir: A web interface for transit/eclipse observability. *Astrophysics Source Code Library* **1306**.007 (2013).
42. Collins, K. A., Kielkopf, J. F., Stassun, K. G. & Hessman, F. V. AstroImageJ: image processing and photometric extraction for ultra-precise astronomical light curves. *Astron. J.* **153**, 77 (2017).
43. Tokovinin, A. Ten years of speckle interferometry at SOAR. *Publ. Astron. Soc. Pacific* **130**, 035002 (2018).
44. Ziegler, C. et al. SOAR TESS Survey. I: sculpting of TESS planetary systems by stellar companions. *Astron. J.* **159**, 19 (2019).
45. Hormuth, F., Brandner, W., Hippler, S. & Henning, T. AstraLux – the Calar Alto 2.2-m telescope LuckyImaging camera. *J. Phys. Conf. Ser.* **131**, 012051 (2008).
46. Fried, D. L. Probability of getting a lucky short-exposure image through turbulence. *J. Opt. Soc. Am.* **68**, 1651–1658 (1978).
47. Strehl, K. Über die Bildschärfe der Fernrohre. *Astron. Nachr.* **158**, 89–90 (1902).
48. Lillo-Box, J., Barrado, D. & Bouy, H. Multiplicity in transiting planet-host stars. A lucky imaging study of Kepler candidates. *Astron. Astrophys.* **546**, A10 (2012).
49. Lillo-Box, J., Barrado, D. & Bouy, H. High-resolution imaging of Kepler planet host candidates. A comprehensive comparison of different techniques. *Astron. Astrophys.* **566**, A103 (2014).
50. Howell, S. B., Everett, M. E., Sherry, W., Horch, E. & Ciardi, D. R. Speckle camera observations for the NASA Kepler Mission Follow-up Program. *Astron. J.***142**, 19 (2011).
51. Sousa, S. G. et al. A new procedure for defining a homogenous line-list for solar-type stars. *Astron. Astrophys.* **561**, A21 (2014).
52. Santos, N. C. et al. SWEET-Cat: a catalogue of parameters for Stars With ExoplanETs. I. New atmospheric parameters and masses for 48 stars with planets. *Astron. Astrophys.* **556**, A150 (2013).
53. Sousa, S. G., Santos, N. C., Israelian, G., Mayor, M. & Monteiro, M. J. P. F. G. A new code for automatic determination of equivalent widths: Automatic Routine for line Equivalent widths in stellarSpectra (ARES). *Astron. Astrophys.* **469**, 783–791 (2007).
54. Sousa, S. G., Santos, N. C., Adibekyan, V., Delgado-Mena, E. & Israelian, G. ARES v2: new features and improved performance. *Astron. Astrophys.* **577**, A67 (2015).
55. Kurucz, R. L. *SYNTHE Spectrum Synthesis Programs and Line Data CD-ROM* (Smithsonian Astrophysical Observatory, 1993).
56. Sneden, C. A. *Carbon and Nitrogen Abundances in Metal-Poor Stars. PhD thesis*, Univ. of Texas at Austin (1973).
57. Adibekyan, V. Z. et al. Chemical abundances and kinematics of 257 G-, K-type field giants. Setting a base for further analysis of giant-planet properties orbiting evolved stars. *Mon. Not. R. Astron. Soc.* **450**, 1900–1915 (2015).
58. Adibekyan, V. Z. et al. Chemical abundances of 1111 FGK stars from the HARPS GTO planet search program. Galactic stellar populations and planets. *Astron. Astrophys.* **545**, A32 (2012).
59. Díaz, R. F. et al. PASTIS: Bayesian extrasolar planet validation – I. General framework, models, and performance. *Mon. Not. R. Astron. Soc.* **441**, 983–1004 (2014).
60. Henden, A. A., Levine, S., Terrell, D. & Welch, D. L. APASS – the latest data release. In *American Astronomical Society Meeting Abstracts* Vol. 225, 336.16 (2015).
61. Munari, U. et al. APASS Landolt-Sloan BVgri photometry of RAVE Stars. I. Data, effective temperatures, and reddenings. *Astron. J.* **148**, 81 (2014).
62. Cutri, R. M. & et al. VizieR Online Data Catalog: AllWISE Data Release (Cutri+ 2013) 2328 http://vizier.u-strasbg.fr/viz-bin/VizieR?-source=II/328 (2014).
63. Southworth, J. Homogeneous studies of transiting extrasolar planets - I. Light-curve analyses. *Mon. Not. R. Astron. Soc.* **386**, 1644–1666 (2008).
64. Kipping, D. M. Binning is sinning: morphological light-curve distortions due to finite integration time. *Mon. Not. R. Astron. Soc.* **408**, 1758–1769 (2010).
65. Allard, F., Homeier, D. & Freytag, B. Models of very-low-mass stars, brown dwarfs and exoplanets. *Philos. Trans. Royal Soc. A* **370**, 2765–2777 (2012).
66. Dotter, A. et al. The Dartmouth stellar evolution database. Astrophys. *J. Suppl. Ser.* **178**, 89–101 (2008).
67. Kipping, D. M. Characterizing distant worlds with asterodensity profiling. *Mon. Not. R. Astron. Soc.* **440**, 2164–2184 (2014).
68. Schönrich, R., McMillan, P. & Eyer, L. Distances and parallax bias in Gaia DR2. *Mon. Not. R. Astron. Soc.* **487**, 3568–3580 (2019).
69. Van Eylen, V. et al. The orbital eccentricity of small planet systems. *Astron. J.* **157**, 61 (2019).
70. Claret, A. & Bloemen, S. Gravity and limb-darkening coefficients for the Kepler, CoRoT, Spitzer, uvby, UBVRIJHK, and Sloan photometric systems. *Astron. Astrophys.* **529**, A75 (2011).
71. Stassun, K. G. & Torres, G. Eclipsing binaries as benchmarks for trigonometric parallaxes in the Gaia era. *Astron. J.* **152**, 180 (2016).
72. Stassun, K. G., Corsaro, E., Pepper, J. A. & Gaudi, B. S. Empirical accurate masses and radii of single stars with TESS and Gaia. *Astron. J.* **155**, 22 (2018).
73. Schlegel, D. J., Finkbeiner, D. P. & Davis, M. Maps of dust infrared emission for use in estimation of reddening and cosmic microwave background radiation foregrounds. *Astrophys. J.* **500**, 525–553 (1998).
74. Stassun, K. G. & Torres, G. Evidence for a systematic offset of −80 μas in the Gaia DR2 parallaxes. *Astrophys. J.* **862**, 61 (2018).
75. Torres, G., Andersen, J. & Giménez, A. Accurate masses and radii of normal stars: modern results and applications. *Astron. Astrophys.* **18**, 67–126 (2010).
76. Hakim, K. et al. A new ab initio equation of state of hcp-Fe and its implication on the interior structure and mass-radius relations of rocky super-Earths. *Icarus* **313**, 61–78 (2018).
77. Connolly, J. A. D. The geodynamic equation of state: what and how. *Geochem. Geophys. Geosyst.* **10**, Q10014 (2009).

78. Vazan, A., Kovetz, A., Podolak, M. & Helled, R. The effect of composition on the evolution of giant and intermediate-mass planets. *Mon. Not. R. Astron. Soc.* **434**, 3283–3292 (2013).
79. Seager, S., Kuchner, M., Hier-Majumder, C. A. & Militzer, B. Mass–radius relationships for solid exoplanets. *Astrophys. J.* **669**, 1279–1297 (2007).
80. Saumon, D., Chabrier, G. & van Horn, H. M. An equation of state for low-mass stars and giant planets. *Astrophys. J. S* **99**, 713 (1995).
81. Dorn, C. et al. Can we constrain the interior structure of rocky exoplanets from mass and radius measurements? *Astron. Astrophys.* **577**, A83 (2015).
82. Lozovsky, M., Helled, R., Rosenberg, E. D. & Bodenheimer, P. Jupiter's formation and its primordial internal structure. *Astrophys. J.* **836**, 227 (2017).
83. Lozovsky, M., Helled, R., Dorn, C. & Venturini, J. Threshold radii of volatile-rich planets. *Astrophys. J.* **866**, 49 (2018).
84. Lammer, H. et al. Atmospheric loss of exoplanets resulting from stellar X-Ray and extreme-ultraviolet heating. *Astrophys. J. Lett.* **598**, 121–124 (2003).
85. Jackson, A. P., Davis, T. A. & Wheatley, P. J. The coronal X-ray-age relation and its implications for the evaporation of exoplanets. *Mon. Not. R. Astron. Soc.* **422**, 2024–2043 (2012).
86. King, G. W. et al. The XUV environments of exoplanets from Jupiter-size to super-Earth. *Mon. Not. R. Astron. Soc.* **478**, 1193–1208 (2018).
87. Chadney, J. M., Galand, M., Unruh, Y. C., Koskinen, T. T. & Sanz-Forcada, J. XUV-driven mass lossfrom extrasolar giant planets orbiting active stars. *Icarus* **250**, 357–367 (2015).
88. Watson, A. J., Donahue, T. M. & Walker, J. C. G. The dynamics of a rapidly escaping atmosphere: applications to the evolution of Earth and Venus. *Icarus* **48**, 150–166 (1981).
89. Erkaev, N. V. et al. Roche lobe effects on the atmospheric loss from "Hot Jupiters". *Astron. Astrophys.* **472**, 329–334 (2007).
90. Kubyshkina, D. et al. Grid of upper atmosphere models for 1–40 $M_{\oplus}$ planets: application to CoRoT-7b and HD 219134b,c. *Astron. Astrophys.* **619**, A151 (2018).
91. Kubyshkina, D. et al. Overcoming the limitations of the energy-limited approximation for planet atmospheric escape. *Astrophys. J. Lett.* **866**, 18 (2018).
92. Madhusudhan, N. & Winn, J. N. Empirical constraints on trojan companions and orbital eccentricities in 25 transiting exoplanetary systems. *Astrophys. J.* **693**, 784–793 (2009).
93. Ford, E. B. & Gaudi, B. S. Observational constraints on trojans of transiting extrasolar planets. *Astrophys. J. Lett.* **652**, 137–140 (2006).
94. Janson, A. Systematic search for trojan planets in the Kepler data. *Astrophys. J.* **774**, 156 (2013).
95. Lillo-Box, J. et al. The TROY project: searching for co-orbital bodies to known planets. I. Project goals and first results from archival radial velocity. *Astron. Astrophys.* **609**, A96 (2018).
96. Lillo-Box, J. et al. The TROY project. II. Multi-technique constraints on exotrojans in nine planetary systems. *Astron. Astrophys.* **618**, A42 (2018).
97. Lillo-Box, J. et al. Kepler-91b: a planet at the end of its life. Planet and giant host star properties via lightcurve variations. *Astron. Astrophys.* **562**, A109 (2014).
98. Leleu, A. et al. Co-orbital exoplanets from close period candidates: the TOI-178 case. *Astron. Astrophys.* **624** A46 (2019).
99. Laughlin, G. & Chambers, J. E. Extrasolar trojans: the viability and detectability of planets in the 1:1 resonance. *Astron. J.* **124**, 592–600 (2002).
100. Leleu, A., Robutel, P., Correia, A. C. M. & Lillo-Box, J. Detection of co-orbital planets by combining transit and radial-velocity measurements. *Astron. Astrophys.* **599**, L7 (2017).
101. Foreman-Mackey, D., Hogg, D. W., Lang, D. & Goodman, J. emcee: the MCMC hammer. *Publ. Astron. Soc. Pacif.* **125**, 306–312 (2013).
102. Kane, S. R. Worlds without moons: exomoon constraints for compact planetary systems. *Astrophys. J. Lett.* **839**, L19 (2017).
103. Lynden-Bell, D. & Pringle, J. E. The evolution of viscous discs and the origin of the nebular variables. *Mon. Not. R. Astron. Soc.* **168**, 603–637 (1974).
104. Shakura, N. I. & Sunyaev, R. A. Black holes in binary systems. Observational appearance. *Astron. Astrophys.* **500**, 33–51 (1973).
105. Nakamoto, T. & Nakagawa, Y. Formation, early evolution, and gravitational stability of protoplanetary disks. *Astrophys. J.* **421**, 640 (1994).
106. Hueso, R. & Guillot, T. Evolution of protoplanetary disks: constraints from DM Tauri and GM Aurigae. *Astron. Astrophys.* **442**, 703–725 (2005).
107. Baraffe, I., Homeier, D., Allard, F. & Chabrier, G. New evolutionary models for pre-main sequence and main sequence low-mass stars down to the hydrogen-burning limit. *Astron. Astrophys.* **577**, A42 (2015).
108. Clarke, C. J., Gendrin, A. & Sotomayor, M. The dispersal of circumstellar discs: the role of the ultraviolet switch. *Mon. Not. R. Astron. Soc.* **328**, 485–491 (2001).
109. Matsuyama, I., Johnstone, D. & Hartmann, L. Viscous diffusion and photoevaporation of stellar disks. *Astrophys. J.* **582**, 893–904 (2003).
110. Ida, S. & Makino, J. Scattering of planetesimals by a protoplanet: slowing down of runaway growth. *Icarus* **106**, 210–227 (1993).
111. Ohtsuki, K., Stewart, G. R. & Ida, S. Evolution of planetesimal velocities based on three-body orbital integrations and growth of protoplanets. *Icarus* **155**, 436–453 (2002).
112. Thommes, E. W., Duncan, M. J. & Levison, H. F. Oligarchic growth of giant planets. *Icarus* **161**, 431–455 (2003).
113. Inaba, S. & Ikoma, M. Enhanced collisional growth of a protoplanet that has an atmosphere. *Astron. Astrophys.* **410**, 711–723 (2003).
114. Bodenheimer, P. & Pollack, J. B. Calculations of the accretion and evolution of giant planets: the effects of solid cores. *Icarus* **67**, 391–408 (1986).
115. Pollack, J. B. et al. Formation of the giant planets by concurrent accretion of solids and gas. *Icarus* **124**, 62–85 (1996).
116. Lee, E. J. & Chiang, E. To cool is to accrete: analytic scalings for nebular accretion of planetary atmospheres. *Astrophys. J.* **811**, 41 (2015).
117. Bodenheimer, P., Hubickyj, O. & Lissauer, J. J. Models of the in situ formation of detected extrasolar giant planets. *Icarus* **143**, 2–14 (2000).
118. Chambers, J. E. A hybrid symplectic integrator that permits close encounters between massive bodies. *Mon. Not. R. Astron. Soc.* **304**, 793–799 (1999).
119. Broeg, C. H. & Benz, W. Giant planet formation: episodic impacts versus gradual core growth. *Astron. Astrophys.* **538**, A90 (2012).
120. Coleman, G. A. L. & Nelson, R. P. On the formation of planetary systems via oligarchic growth in thermally evolving viscous discs. *Mon. Not. R. Astron. Soc.* **445**, 479–499 (2014).
121. Paardekooper, S. J., Baruteau, C. & Kley, W. A torque formula for non-isothermal Type I planetary migration - II. Effects of diffusion. *Mon. Not. R. Astron. Soc.* **410**, 293–303 (2011).
122. Fendyke, S. M. & Nelson, R. P. On the corotation torque for low-mass eccentric planets. *Mon. Not. R. Astron. Soc.* **437**, 96–107 (2014).
123. Dittkrist, K. M., Mordasini, C., Klahr, H., Alibert, Y. & Henning, T. Impacts of planet migration models on planetary populations. Effects of saturation, cooling and stellar irradiation. *Astron. Astrophys.* **567**, A121 (2014).
124. Jin, S. et al. Planetary population synthesis coupled with atmospheric escape: a statistical view of evaporation. *Astrophys. J.* **795**, 65 (2014).
125. Jin, S. & Mordasini, C. Compositional imprints in density-distance-time: a rocky composition for close-in low-mass exoplanets from the location of the valley of evaporation. *Astrophys. J.* **853**, 163 (2018).
126. Benítez-Llambay, P., Masset, F. & Beaugé, C. The mass-period distribution of close-in exoplanets. *Astron. Astrophys.* **528**, A2 (2011).
127. Mordasini, C., Alibert, Y. & Benz, W. Extrasolar planet population synthesis. I. Method, formation tracks, and mass-distance distribution. *Astron. Astrophys.* **501**, 1139–1160 (2009).
128. Tychoniec, L. et al. The VLA Nascent Disk and Multiplicity Survey of Perseus Protostars (VANDAM). IV. Free–free emission from protostars: links to infrared properties, outflow tracers, and protostellar disk masses. *Astrophys. J. Suppl. Ser.* **238**, 19 (2018).
129. Andrews, S. M., Wilner, D. J., Hughes, A. M., Qi, C. & Dullemond, C. P. Protoplanetary disk structures in Ophiuchus. II. Extension to fainter sources. *Astrophys. J.* **723**, 1241–1254 (2010).
130. Venuti, L. et al. CSI 2264: investigating rotation and its connection with disk accretion in the young open cluster NGC 2264. *Astron. Astrophys.* **599**, A23 (2017).
131. Lodders, K. Solar system abundances and condensation temperatures of the elements. *Astrophys. J.* **591**, 1220–1247 (2003).
132. Ansdell, M. et al. ALMA survey of Lupus protoplanetary disks. II. Gas disk radii. *Astrophys. J.* **859**, 21 (2018).
133. Ivanov, P. B. & Papaloizou, J. C. B. On the tidal interaction of massive extrasolar planets on highly eccentric orbits. *Mon. Not. R. Astron. Soc.* **347**, 437–453 (2004).
134. Vick, M. & Lai, D. Dynamical tides in highly eccentric binaries: chaos, dissipation, and quasi-steady state. *Mon. Not. R. Astron. Soc.* **476**, 482–495 (2018).
135. Wu, Y. Diffusive tidal evolution for migrating hot Jupiters. *Astron. J.* **155**, 118 (2018).
136. Vick, M., Lai, D. & Anderson, K. R. Chaotic tides in migrating gas giants: forming hot and transient warm Jupiters via Lidov–Kozai migration. *Mon. Not. R. Astron. Soc.* **484**, 5645–5668 (2019).
137. Veras, D. & Fuller, J. Tidal circularization of gaseous planets orbiting white dwarfs. *Mon. Not. R. Astron. Soc.* **489**, 2941–2953 (2019).
138. Tinetti, G. et al. A chemical survey of exoplanets with ARIEL. *Exp. Astron.* **46**, 135–209 (2018).
139. Stassun, K. G. et al. The revised TESS input catalog and candidate target list. *Astron. J.* **158**, 138 (2019).
140. Skrutskie, M. F. et al. The Two Micron All Sky Survey (2MASS). *Astron. J.* **131**, 1163–1183 (2006).

Acknowledgements This paper includes data collected by the TESS missions, which are publicly available from MAST. Funding for the TESS mission is provided by NASA's Science Mission directorate. We acknowledge the use of public TESS Alert data from pipelines at the TESS Science Office and at the TESS Science Processing Operations Center. Resources supporting this work were provided by the NASA High-End Computing (HEC) Program through the NASA Advanced Supercomputing (NAS) Division at Ames Research Center for the production of the SPOC data products. This research made use of the Exoplanet Follow-up Observation Program website and the NASA Exoplanet Archive, which are operated by the California Institute of Technology, under contract with the National Aeronautics and Space Administration under the Exoplanet Exploration Program. This work makes use of observations from the LCOGT network and is based in part on observations collected at the European Organisation for Astronomical Research in the Southern Hemisphere under ESO programme IDs 1102.C-0249 and P103.C-0449. Some of the observations presented in the paper used the High-Resolution Imaging instrument Zorro at Gemini South (programme ID GS-2019B-Q-111). Zorro was funded by the NASA Exoplanet Exploration Program and built at the NASA Ames Research Center by S.B.H., N. Scott, E. P. Horch and E. Quigley. D.J.A., D.V. and S.L.C. acknowledge support from the STFC via Ernest Rutherford Fellowships ST/R00384X/1, ST/P003850/1 and ST/R003726/1, respectively. M.B. and S.Gandhi acknowledge support from the STFC research grant ST/S000631/1. G.M.K. is supported by the Royal Society as a Royal Society University Research Fellow. F.M. acknowledges support from a Royal Society Dorothy Hodgkin Fellowship. K.G.S. acknowledges partial support from NASA grant 17-XRP17 2-0024. C.Z. is supported by a Dunlap Fellowship at the Dunlap Institute for Astronomy and Astrophysics, funded through an endowment established by the Dunlap family and the University of Toronto. A.W.M. was supported by NASA grant 80NSSC19K0097 to the University of North Carolina at Chapel Hill. D.J.A.B. acknowledges support from the UK Space Agency. C.X.H. and M.N.G. acknowledge support from the Juan Carlos Torres Fellowship. This work was financed by FEDER (Fundo Europeu de Desenvolvimento Regional) funds through the COMPETE 2020 Operational Programme for Competitiveness and Internationalisation (POCI) and by Portuguese funds through FCT (Fundação para a Ciência e a Tecnologia) in the framework of projects UID/FIS/04434/2019; PTDC/FIS-AST/32113/2017 and POCI-01-0145-FEDER-032113; PTDC/FIS-AST/28953/2017 and POCI-01-0145-FEDER-028953. S.G.S., V.A., S.C.C.B. and O.D.S.D. acknowledge support from FCT through Investigador FCT contracts IF/00028/2014/CP1215/CT0002, IF/00650/2015/CP1273/CT0001, IF/01312/2014/CP1215/CT0004 and DL 57/2016/CP1364/CT0004. S.H. acknowledges support from fellowships PD/BD/128119/2016 funded by FCT (Portugal). Work by J.N.W. was partly funded by the Heising-Simons Foundation. C.A.W. acknowledges support from UK Science Technology and Facility Council grant ST/P000312/1. J.L.-B. and D. Barrado are funded by the Spanish State

Research Agency (AEI) Projects ESP2017-87676-C5-1-R and MDM-2017-0737 Unidad de Excelencia María de Maeztu – Centro de Astrobiología (INTA-CSIC). J.S.J. acknowledges funding by Fondecyt through grant 1161218 and partial support from CATA-Basal (PB06, Conicyt). J.I.V. acknowledges support from CONICYT-PFCHA/Doctorado Nacional-21191829, Chile. The French group acknowledges financial support from the French Programme National de Planétologie (PNP, INSU). F.M. acknowledges support from the Royal Society Dorothy Hodgkin Fellowship. C.M. and A.E. acknowledge support from the Swiss National Science Foundation under grant BSSGI0_155816 "PlanetsInTime". Parts of this work have been carried out within the framework of the NCCR PlanetS supported by the Swiss National Science Foundation.

Author contributions D.J.A. is Principal Investigator of the NCORES HARPS programme, which measured the planet's mass, and a member of the NGTS consortium; D.J.A. developed much of the text and main figures and coordinated all contributions. T.A.L. performed the joint PASTIS analysis. V.A., S.G.S. and N.C.S. performed stellar spectral analysis including chemical abundances. R.A.B. and F.M. provided text analysing potential formation scenarios. K.A.C. and E.L.N.J. coordinated the TFOP SG1 photometric follow-up of the system. K.I.C. and T.G. performed analysis of the LCOGT photometric follow-up of the system. A.E. and C.M. applied and analysed the Bern Population Synthesis Models. C.X.H. and L.S. developed and ran the MIT Quick Look Pipeline, which identified the candidate in the TESS data. G.W.K. performed the photoevaporation analysis. J.L.-B. obtained and analysed the Astralux data and synthesized all high-resolution imaging results. E.M. obtained the NaCo imaging data. H.O. contributed to the NCORES HARPS programme and the NGTS survey and helped to create the main figures. J.O., O.M., M.D., R.H., M. Lozovsky and C.D. performed the interior-structure calculations. D.V. performed analysis on the potential for tidal self-disruption. C.Z. obtained the SOAR data and provided text summarising the SOAR results. T.-G.T. obtained a further transit with the PEST telescope. J.J.L. contributed to the internal structure discussion. K.G.S. provided the independent check of stellar parameters. M.B. and S. Gandhi calculated estimates of the required telescope time for atmospheric characterization. D.R.A., M.M., E.M.B., C.A.W., J.S.J., J.I.V., J.S.A., D. Bayliss, C. Belardi, M.R.B., S.L.C., A.C., P.E., S. Gill, M.R.G., M.N.G., M. Lendl, J.M., D.P., D.Q., L.R., R.H.T. and R.G.W. contributed to the NGTS facility, in planning, management, data collection or detrending. D.J.A.B., S.H., D. Barrado, S.C.C.B., P.A.W., L.D.N., D. Bayliss, F.B., B.F.C., R.F.D., O.D.S.D., X.D., P.F., J.J., G.M.K., A.S., S.U., P.A.W., J.M.A. and A.O. contributed to the HARPS large programme under which the HARPS data were obtained. D.R.C., I.J.M.C., J.E.S. and S.B.H. contributed to the NaCo imaging data. C. Briceño, N.L. and A.W.M. contributed to the SOAR imaging data. K.D.C., M.F., J.S.J., E.L.N.J., G.R.R., P.R., S.S., E.T., R.V., J.N.W., J.N.V. and Z.Z. provided essential contributions to the TESS mission, which discovered the candidate. All authors read the manuscript and provided general comments.

Competing interests The authors declare no competing interests.

Additional information

Correspondence and requests for materials should be addressed to D.J.A.

Peer review information *Nature* thanks Roman Baluev and the other, anonymous, reviewer(s) for their contribution to the peer review of this work.

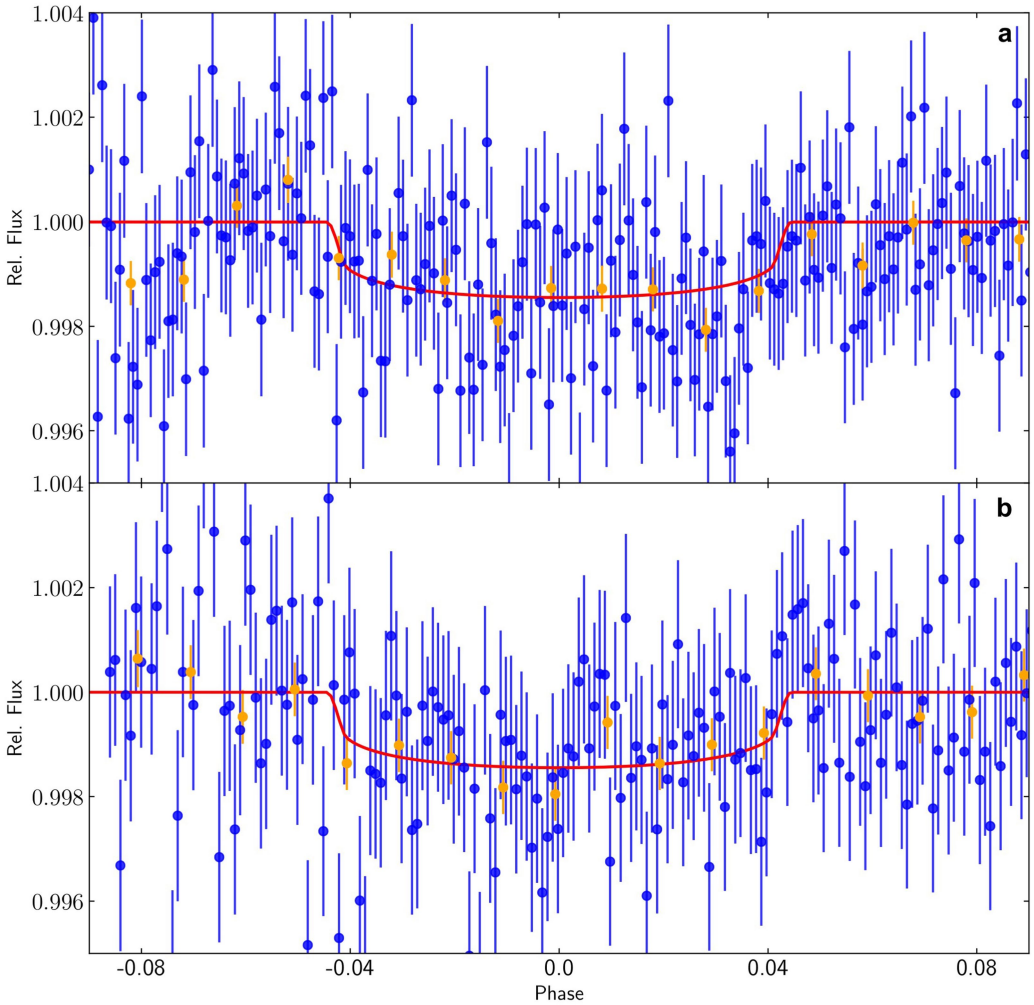

Extended Data Fig. 1 | Photometric data captured by the LCOGT network. **a**, **b**, Data captured on the nights of 30 July 2019 UT (**a**) and 9 August 2019 UT (**b**). The best-fitting model is plotted in red and the binned data in orange. Error bars of individual points show one standard deviation. In the case of binned measurements, points and error bars show the weighted mean and its standard error, respectively.

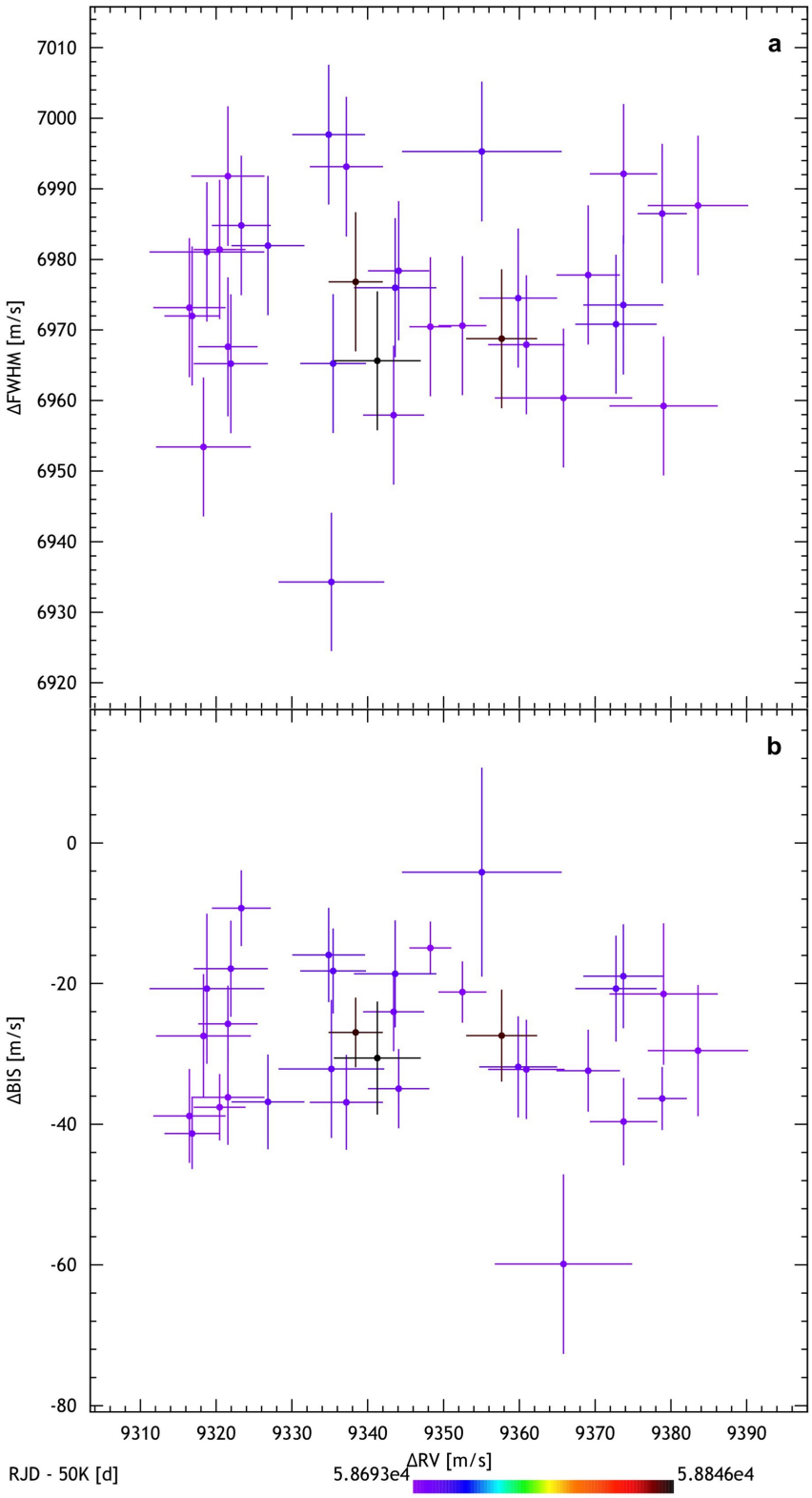

Extended Data Fig. 2 | HARPS activity correlation indicators. a, HARPS radial velocities plotted against their bisector value. Colours represent the time of observation measured in BJD−2,400,000. **b**, As for **a**, for the FWHM of the CCF. No correlation is seen in either case. All error bars show one standard deviation.

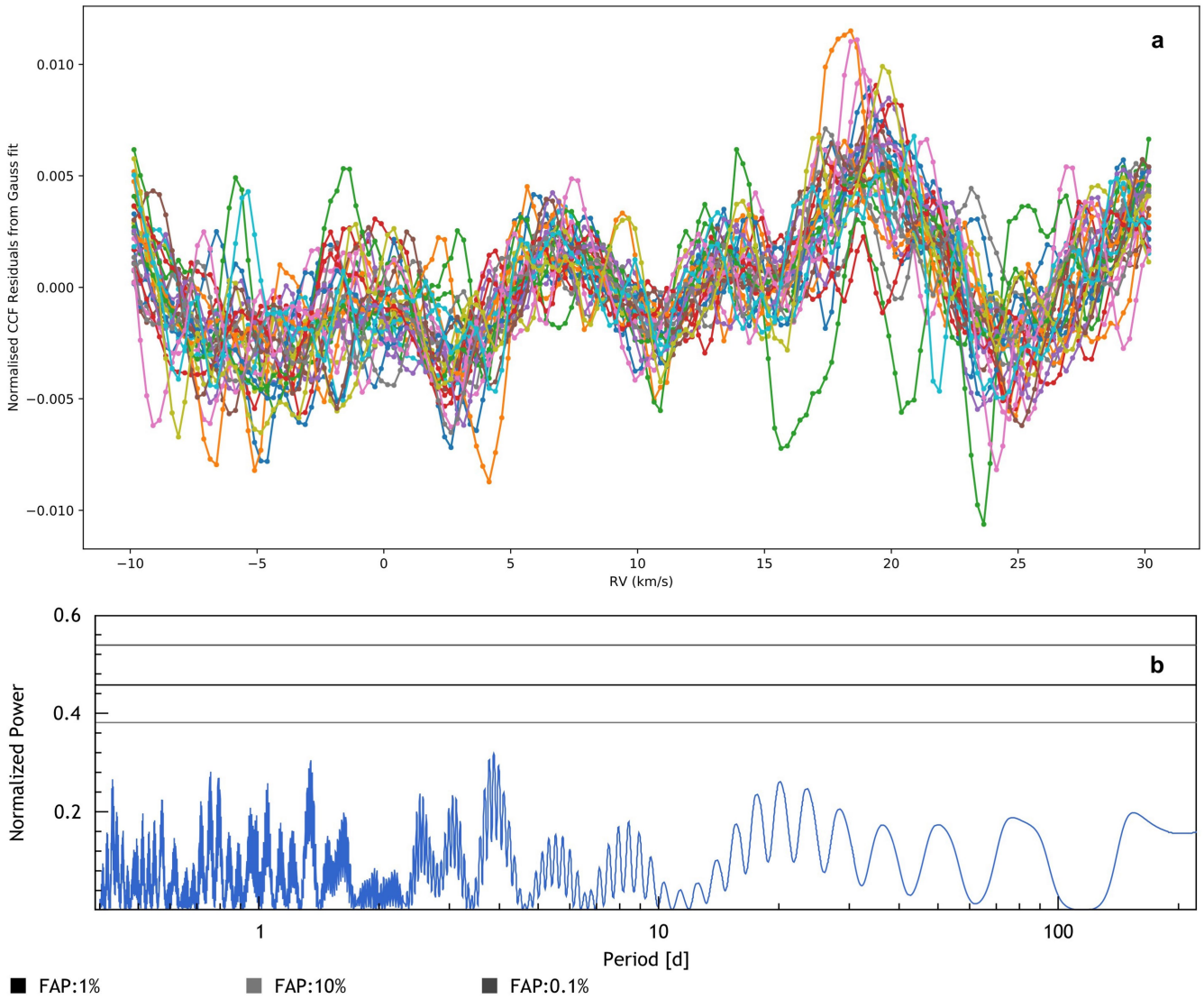

Extended Data Fig. 3 | Tests on the HARPS residuals. a, CCF for the HARPS spectra computed using a G2V template. A Gaussian fit has been removed to leave the residual noise. No clear evidence of a contaminating star is seen. **b**, Periodogram of the HARPS RV residuals. No evidence of periodic structure is found. FAP represents false-alarm probability.

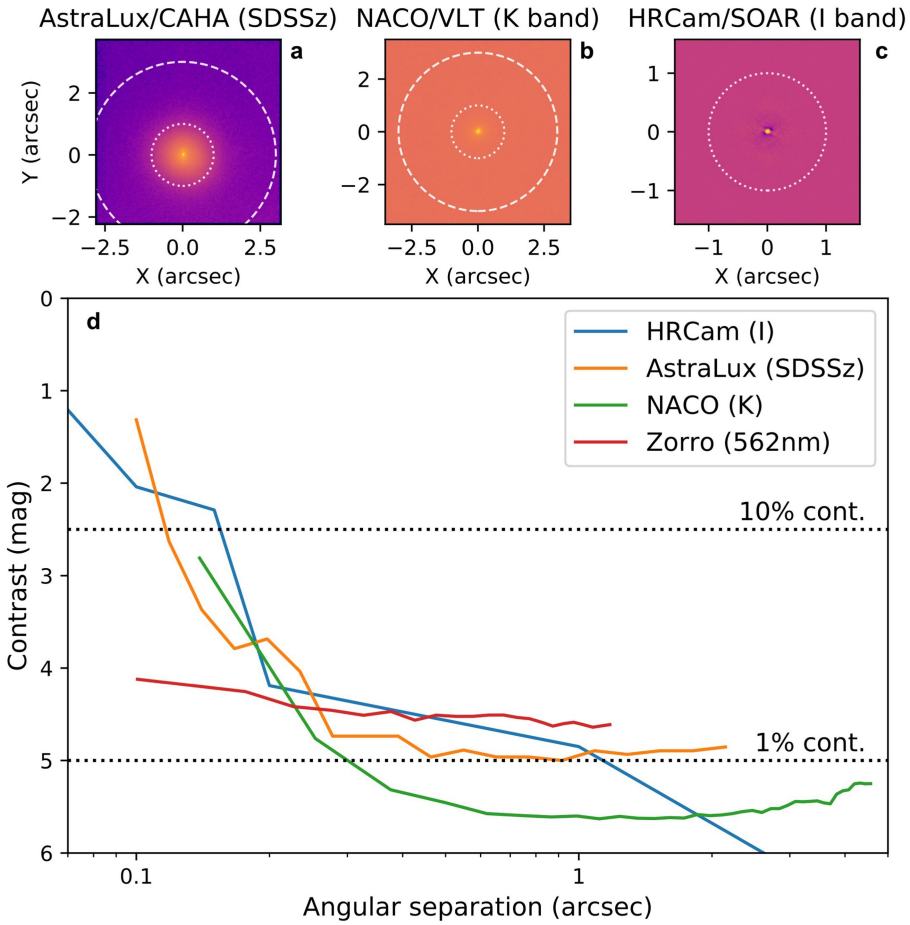

Extended Data Fig. 4 | Collected high-resolution imaging results from AstraLux/CAHA, NaCo/VLT, HRCam/SOAR and Zorro/Gemini (562 nm). **a**–**c**, Images from AstraLux (**a**), NaCo (**b**) and HRCam (**c**). **d**, Sensitivity curves for **a**–**c** and the Zorro 562-nm observation. Our simultaneous 832-nm Zorro observation provides a similar result. The 1% and 10% contrast curves are also plotted.

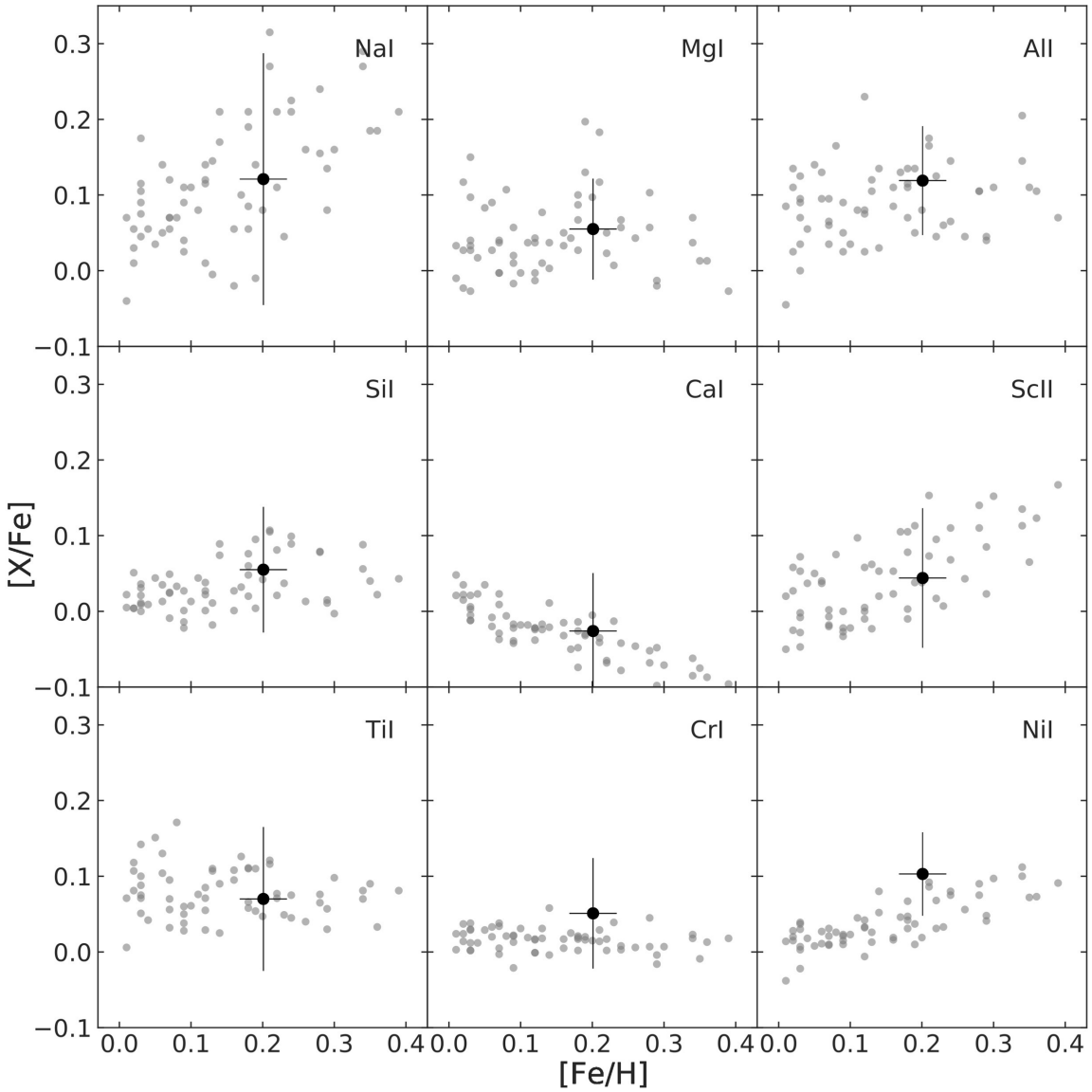

Extended Data Fig. 5 | TOI-849 compared to field stars. Abundance ratio [X/Fe] against stellar metallicity for TOI-849 (black) and for field stars from the HARPS sample (grey) with similar stellar parameters: $T_{\rm eff}$ = 5,329 ± 200 K, log$g$ = 4.28 ± 0.20 dex and [Fe/H] = +0.20 ± 0.20 dex. All error bars show one standard deviation.

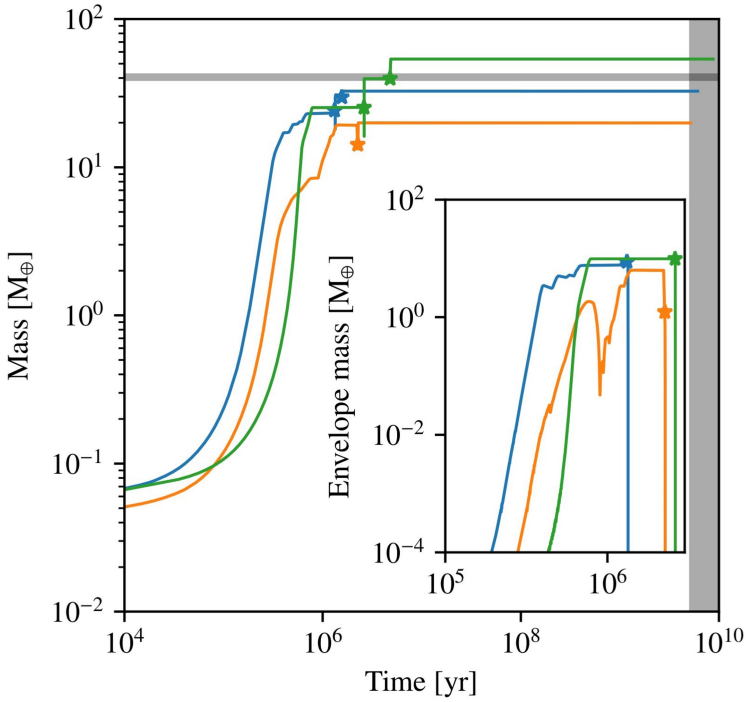

Extended Data Fig. 6 | Planet mass against time for three similar planets to TOI-849b in the Bern Population Synthesis models. Grey shaded regions mark the parameters of TOI-849b. Stars mark the time of a giant impact. The inset shows the envelope mass, which is removed after collision.

Extended Data Table 1 | List of stellar and planetary parameters used in the analysis

Parameter	Prior	Posterior	
		Dartmouth (adopted)	PARSEC
Stellar Parameters			
Effective temperature $T_{\rm eff}$ [K]	$\mathcal{N}(5329.0, 48.0)$	$5373.8^{+42.5}_{-41.2}$	$5377.0^{+40.5}_{-39.9}$
Surface gravity log g [cgs]	$\mathcal{N}(4.43, 0.3)$	$4.48^{+0.03}_{-0.04}$	$4.47^{+0.03}_{-0.04}$
Iron abundance [Fe/H] [dex]	$\mathcal{N}(0.201, 0.033)$	0.19 ± 0.03	0.2 ± 0.03
Distance to Earth D [pc]	$\mathcal{N}(224.56, 7.1)$	$224.9^{+5.9}_{-5.5}$	$224.7^{+6.2}_{-5.8}$
Interstellar extinction $E(B-V)$ [mag]	$\mathcal{U}(0.0, 1.0)$	$0.011^{+0.016}_{-0.008}$	$0.01^{+0.016}_{-0.008}$
Systemic radial velocity γ [km s^{-1}]	$\mathcal{U}(5.0, 15.0)$	$9.3502^{+0.0014}_{-0.0013}$	$9.3503^{+0.0014}_{-0.0013}$
Limb-darkening u_a	(derived)	$0.3766^{+0.007}_{-0.0071}$	$0.376^{+0.0069}_{-0.0071}$
Limb-darkening u_b	(derived)	$0.2385^{+0.0041}_{-0.004}$	$0.2389^{+0.004}_{-0.0039}$
Stellar density $\rho_\star/\rho_\odot$	(derived)	$1.195^{+0.118}_{-0.123}$	$1.175^{+0.118}_{-0.140}$
Stellar mass $M_\star$ [$M_\odot$]	(derived)	$0.929^{+0.023}_{-0.023}$	$0.901^{+0.027}_{-0.026}$
Stellar radius $R_\star$ [$R_\odot$]	(derived)	$0.919^{+0.029}_{-0.023}$	$0.916^{+0.031}_{-0.023}$
Stellar age τ [Gyr]	(derived)	$6.7^{+2.9}_{-2.4}$	$8.6^{+3.4}_{-2.9}$
Planet b Parameters			
Orbital Period P_b [d]	$\mathcal{N}(0.76552484, 4.35e-06)$	$0.76552414^{+0.00000262}_{-0.00000279}$	$0.76552402^{+0.00000262}_{-0.00000280}$
Epoch $T_{0,b}$ [BJD - 2450000]	$\mathcal{N}(8394.73741796, 0.0017159129)$	$8394.73768^{+0.00091}_{-0.00099}$	$8394.73768^{+0.00098}_{-0.00096}$
RV semi-amplitude K_b [km s^{-1}]	$\mathcal{U}(0.0, 0.1)$	$0.02864^{+0.00187}_{-0.00182}$	$0.02862^{+0.00198}_{-0.00179}$
Orbital inclination i_b [°]	$\mathcal{S}(50.0, 90.0)$	$86.8^{+2.1}_{-2.4}$	$86.4^{+2.4}_{-2.7}$
Planet-to-star radius ratio k_b	$\mathcal{U}(0.0, 1.0)$	$0.03443^{+0.00092}_{-0.00088}$	$0.03445^{+0.00093}_{-0.00093}$
Orbital eccentricity e_b	$\mathcal{T}(0.0, 0.083, 0.0, 1.0)$	0.0 ± 0.0	0.0 ± 0.0
Argument of periastron ω_b [°]	$\mathcal{U}(0.0, 360.0)$	0.0 ± 0.0	0.0 ± 0.0
System scale $a_b/R_\star$	(derived)	$3.7^{+0.1}_{-0.1}$	$3.7^{+0.1}_{-0.2}$
Impact parameter b_b	(derived)	$0.212^{+0.145}_{-0.140}$	$0.233^{+0.158}_{-0.156}$
Transit duration $T_{14,b}$ [h]	(derived)	1.57 ± 0.04	1.57 ± 0.04
Semi-major axis a_b [AU]	(derived)	$0.01598^{+0.00013}_{-0.00014}$	$0.01582^{+0.00016}_{-0.00015}$
Planet mass M_b [$M_\oplus$]	(derived)	$39.09^{+2.66}_{-2.55}$	$38.33^{+2.70}_{-2.53}$
Planet radius R_b [$R_\oplus$]	(derived)	$3.444^{+0.157}_{-0.115}$	$3.435^{+0.179}_{-0.130}$
Planet bulk density ρ_b [g cm^{-3}]	(derived)	$5.2^{+0.7}_{-0.8}$	$5.2^{+0.8}_{-0.8}$

The respective priors are provided together with the posteriors for the Dartmouth and PARSEC stellar evolution tracks. The posterior values represent the median and 68.3% credible interval. Derived values that might be useful for follow-up work are also reported. $\mathcal{N}(\mu, \sigma^2)$, normal distribution with mean μ and width σ^2; $\mathcal{U}(a, b)$, uniform distribution between a and b; $\mathcal{S}(a, b)$, sine distribution between a and b ; $\mathcal{T}(\mu, \sigma^2, a, b)$, truncated normal distribution between a and b with mean μ and width σ^2.

Extended Data Table 2 | List of instrument parameters used in the analysis

Parameter	Prior	Posterior	
		Dartmouth (adopted)	PARSEC
Instrument-related Parameters			
HARPS jitter $\sigma_{j,\ \mathrm{RV}}$ [km s^{-1}]	$\mathcal{U}(0.0, 0.1)$	$0.00525^{+0.00137}_{-0.00125}$	$0.00525^{+0.00141}_{-0.00122}$
HARPS drift [km s^{-1}.d^{-1}]	$\mathcal{U}(-0.001, 0.001)$	$-0.000043^{\pm}0.000031$	-0.000042 ± 0.000030
TESS contamination [%]	$\mathcal{T}(0.0, 0.005, 0.0, 1.0)$	$0.004^{+0.003}_{-0.003}$	$0.003^{+0.004}_{-0.002}$
TESS jitter $\sigma_{j,\ TESS}$ [ppm]	$\mathcal{U}(0.0, 10^5)$	$53.0^{+51.8}_{-36.1}$	$53.0^{+52.5}_{-37.8}$
TESS out-of-transit flux	$\mathcal{U}(0.99, 1.01)$	$1.0001003^{+0.0000209}_{-0.0000204}$	$1.0001001^{+0.0000218}_{-0.0000212}$
TESS limb-darkening u_a	(derived)	0.3766 ± 0.0071	0.3760 ± 0.0071
TESS limb-darkening u_b	(derived)	0.2385 ± 0.0041	0.2389 ± 0.0040
NGTS$_1$ contamination [%]	$\mathcal{T}(0.0, 0.005, 0.0, 1.0)$	$0.003^{+0.004}_{-0.002}$	$0.003^{+0.004}_{-0.002}$
NGTS$_1$ jitter $\sigma_{j,\ NGTSfirst}$ [ppm]	$\mathcal{U}(0.0, 10^5)$	$71.9^{+84.2}_{-51.7}$	$74.7^{+82.4}_{-52.7}$
NGTS$_1$ out-of-transit flux	$\mathcal{U}(0.99, 1.01)$	$1.0000853^{+0.0000801}_{-0.0000896}$	$1.00008^{+0.0000864}_{-0.0000862}$
NGTS$_2$ contamination [%]	$\mathcal{T}(0.0, 0.005, 0.0, 1.0)$	$0.003^{+0.003}_{-0.002}$	$0.003^{+0.004}_{-0.002}$
NGTS$_2$ jitter $\sigma_{j,\ NGTSsecond}$ [ppm]	$\mathcal{U}(0.0, 10^5)$	$85.1^{+98.7}_{-59.7}$	$84.8^{+97.2}_{-60.2}$
NGTS$_2$ out-of-transit flux	$\mathcal{U}(0.99, 1.01)$	$1.0000869^{+0.0000839}_{-0.0000962}$	$1.0000765^{+0.0000963}_{-0.0000944}$
NGTS limb-darkening u_a	(derived)	0.4758 ± 0.0080	0.4752 ± 0.0081
NGTS limb-darkening u_b	(derived)	0.2114 ± 0.0050	0.2118 ± 0.0050
LCO$_1$ contamination [%]	$\mathcal{T}(0.0, 0.005, 0.0, 1.0)$	$0.003^{+0.004}_{-0.002}$	$0.003^{+0.004}_{-0.002}$
LCO$_1$ jitter $\sigma_{j,\ LCOsecond}$ [ppm]	$\mathcal{U}(0.0, 10^5)$	$1022.0^{+85.6}_{-86.9}$	$1022.6^{+88.3}_{-90.2}$
LCO$_1$ out-of-transit flux	$\mathcal{U}(0.98, 1.02)$	$0.9999986^{+0.0000880}_{-0.0000870}$	$0.9999953^{+0.0000870}_{-0.0000879}$
LCO$_2$ contamination [%]	$\mathcal{T}(0.0, 0.005, 0.0, 1.0)$	$0.003^{+0.004}_{-0.002}$	$0.003^{+0.004}_{-0.002}$
LCO$_2$ jitter $\sigma_{j,\ LCOthird}$ [ppm]	$\mathcal{U}(0.0, 10^5)$	$1417.1^{+86.7}_{-76.3}$	$1420.7^{+86.7}_{-84.7}$
LCO$_2$ out-of-transit flux	$\mathcal{U}(0.98, 1.02)$	$0.9999873^{+0.0000947}_{-0.0000976}$	$0.9999938^{+0.0001048}_{-0.0001031}$
LCO limb-darkening u_a	(derived)	0.3828 ± 0.0072	0.3822 ± 0.0073
LCO limb-darkening u_b	(derived)	0.2386 ± 0.0044	0.2390 ± 0.0042
SED jitter [mag]	$\mathcal{U}(0.0, 0.1)$	$0.049^{+0.03}_{-0.026}$	$0.047^{+0.031}_{-0.026}$

The respective priors are provided together with the posteriors for the Dartmouth and PARSEC stellar evolution tracks. The posterior values represent the median and 68.3% credible interval. $\mathcal{N}(\mu, \sigma^2)$, normal distribution with mean μ and width σ^2; $\mathcal{U}(a, b)$, uniform distribution between a and b; $\mathcal{T}(\mu, \sigma^2, a, b)$, truncated normal distribution between a and b with mean μ and width σ^2.

Extended Data Table 3 | Stellar properties of TOI-849

Property	Value	Source
Astrometric Properties		
RA	01:54:51.7910	GAIA DR2
Dec	-29:25:18.1508	GAIA DR2
TIC ID	33595516	TICv8
GAIA ID	5023809953208388352	GAIA DR2
2MASS ID	01545169-2925186	2MASS
μ_{RA} (mas.yr^{-1})	73.315	GAIA DR2
μ_{Dec} (mas.yr^{-1})	20.664	GAIA DR2
Photometric Properties		
TESS (mag)	11.55	TICv8
B (mag)	12.84	TICv8
V (mag)	11.98	TICv8
G (mag)	12.06	TICv8
J (mag)	10.83	TICv8
H (mag)	10.48	TICv8
K (mag)	10.42	TICv8

Sources: Gaia Data Release 2[10], TICv8[139], 2MASS[140].

Extended Data Table 4 | HARPS radial velocities

BJD d	RV kms^{-1}	σ_{RV} kms^{-1}	CCF FWHM kms^{-1}	CCF Contrast	Bisector kms^{-1}	S/N(50)	T_{exp} s	$\mathrm{Airmass}_{\mathrm{start}}$
2458692.78910182	9.320464	0.003341	6.9814	57.568	-0.0376	28.9	1800	1.464
2458692.87197814	9.348264	0.002660	6.9705	57.606	-0.0149	35.0	1800	1.073
2458693.78193905	9.379034	0.007109	6.9592	58.265	-0.0215	16.7	1500	1.49
2458693.86713031	9.383575	0.006590	6.9876	57.935	-0.0295	17.6	1200	1.069
2458694.79485824	9.352493	0.003080	6.9706	57.677	-0.0212	31.2	1500	1.365
2458694.89266609	9.321555	0.004772	6.9918	57.768	-0.0362	22.3	1200	1.022
2458695.76161626	9.316472	0.004716	6.9732	57.804	-0.0388	22.9	1500	1.633
2458695.8578846	9.318335	0.006212	6.9534	58.095	-0.0274	18.1	1200	1.078
2458697.77111987	9.373754	0.004389	6.9921	57.730	-0.0396	24.0	1800	1.508
2458697.86515415	9.365826	0.009028	6.9604	58.639	-0.0599	13.5	1200	1.051
2458698.79553074	9.316836	0.003574	6.9720	57.644	-0.0413	28.1	1500	1.296
2458698.86273442	9.321557	0.003851	6.9676	57.785	-0.0257	26.1	1500	1.055
2458699.77215996	9.343418	0.003958	6.9579	57.855	-0.0240	26.0	1500	1.434
2458699.86782619	9.360927	0.004984	6.9679	57.876	-0.0322	21.5	1200	1.038
2458700.7860712	9.378852	0.003165	6.9865	57.620	-0.0363	30.7	1500	1.321
2458700.86459501	9.369082	0.004117	6.9778	57.755	-0.0324	24.9	1200	1.039
2458701.74930712	9.337185	0.004769	6.9931	57.629	-0.0369	22.8	1200	1.573
2458701.82063133	9.321939	0.004835	6.9652	57.948	-0.0179	21.9	1200	1.139
2458701.91235041	9.318780	0.007543	6.9811	58.274	-0.0207	15.3	1200	1.0
2458702.75424659	9.323328	0.003815	6.9848	57.651	-0.0093	26.7	1200	1.504
2458702.82285066	9.344083	0.003979	6.9784	57.701	-0.0349	25.8	1200	1.125
2458705.75330754	9.335210	0.006936	6.9343	57.874	-0.0321	16.5	1200	1.443
2458705.8276873	9.326840	0.004757	6.9820	57.743	-0.0368	22.3	1200	1.087
2458705.92257763	9.359851	0.005083	6.9745	57.812	-0.0318	21.9	1200	1.007
2458706.89905173	9.373723	0.005230	6.9735	57.873	-0.0190	20.6	1800	1.0
2458707.74440581	9.372752	0.005320	6.9708	57.367	-0.0207	20.7	1800	1.508
2458707.85009529	9.355053	0.010510	6.9953	57.194	-0.0042	12.4	1800	1.036
2458708.72594834	9.334852	0.004742	6.9977	57.107	-0.0159	22.9	1200	1.626
2458708.82117413	9.335439	0.004273	6.9652	57.287	-0.0182	24.4	1200	1.084
2458708.92270817	9.343619	0.005383	6.9760	57.703	-0.0186	20.9	1200	1.013
2458838.6181445	9.357671	0.004621	6.9688	57.643	-0.0274	22.8	1800	1.096
2458840.60848862	9.338411	0.003501	6.9768	57.653	-0.0269	28.3	1800	1.087
2458845.6514276	9.341266	0.005679	6.9656	57.812	-0.0306	20.6	1800	1.322

S/N represents the signal-to-noise ratio. σ_{RV} is the 1σ error on the RV measurements. T_{exp} is the exposure time of the observation.